Stress field model for bond in reinforced concrete ties

Tena Galkovski [*], Jaime Mata-Falcón, Walter Kaufmann

Institute of Structural Engineering (IBK), ETH Zürich, Zürich, Switzerland

ARTICLE INFO

ABSTRACT

The interaction of the reinforcing bars and the surrounding concrete plays an important role in structural concrete as it is decisive for the reinforcing bar anchorage and the load-deformation behaviour, including stiffness and deformation capacity. Therefore, understanding this interaction – commonly known as bond – is highly relevant to a safe and efficient structural concrete design. Bond depends on many parameters, which affect the local reinforcing bar-concrete interface as well as the global load transfer between the reinforcing bars and the surrounding concrete. The latter governs the formation of transverse and longitudinal cracks and the activation of transverse confinement, which are as decisive for bond as the local interface characteristics. Nonetheless, most bond models and code provisions focus on the local interface and merely account for the global configuration by means of empirically calibrated factors accounting, e.g. for good or bad bond conditions in confined or unconfined situations, respectively.

This study investigates the potential of stress fields for modelling bond based on the lower-bound theorem of plasticity theory. Stress fields facilitate the investigation of the local interface and the global load transfer consistently in one model, providing valuable insight into the flow of forces. For simplicity, the fundamental case of a concrete tie reinforced with one deformed steel bar is studied in this paper, superimposing axisymmetric discontinuous stress fields originating at each reinforcing bar rib. Each stress field consists of a triaxial nodal zone adjacent to a rib and a conical compression field that spreads the bond force radially, and is equilibrated along its outer perimeter by axial tensile stresses and confining hoops. The model relies on geometric parameters and basic material properties. The validation against experiments on reinforced concrete ties shows a good correlation between the predicted and observed bond strength and the crack spacing. The predictions can be improved by assigning stiffnesses to the stress field components and requiring interface compatibility, i.e. ensuring contact between the concrete and the reinforcing bar at every rib. Even when assuming a simplified, linearly elastic constitutive behaviour for concrete, the consideration of interface compatibility allows for reproducing the steel strain dependency of the local and average bond stresses and the occurrence and impact of splitting cracks.

1. Introduction

The reliable prediction of bond is essential to the efficient and safe design of reinforced concrete (RC) members as it is highly relevant not only for serviceability, by governing the cracked member behaviour and thus its stiffness, but also for the ultimate limit state, by influencing reinforcement anchorage and the member deformation capacity. A broad consensus exists upon the main bond mechanisms in RC members subjected to uniaxial tension. However, the development of generally applicable, mechanically sound models is hindered by the complex interaction of numerous influencing factors which affect the local reinforcing bar-concrete interfacial behaviour and the load transfer in the surrounding concrete. The local interface behaviour is governed by the interface characteristics, i.e. the diameter, rib pattern and deformations of the reinforcing bars, including their axial strains and relative displacement with respect to the concrete (referred to as bond slip) and the concrete strength. However, it is also strongly affected by the transverse confinement and the formation of transverse and longitudinal cracks. These effects depend on the global configuration of the member, which is characterised by the reinforcement ratio, the reinforcing bar spacing, the concrete cover thickness, transverse reinforcement if present, and the concrete strength, and governs the load transfer to the surrounding concrete. Hence, the global configuration is as decisive for the load transfer between reinforcing bars and concrete as the local interface characteristics.

Nonetheless, existing bond models and modern design codes [1–3] typically focus on the local force transfer between reinforcing bars and

---

* Corresponding author.
E-mail addresses: galkovski@ibk.baug.ethz.ch (T. Galkovski), mata-falcon@ibk.baug.ethz.ch (J. Mata-Falcón), kaufmann@ibk.baug.ethz.ch (W. Kaufmann).

Nomenclature

c	cohesion
f_{c0}	uniaxial concrete compressive strength
f_{ctm}	mean concrete tensile strength
f_R	relative rib area
f_{su}	steel ultimate stress
f_{sy}	steel yield stress
h_R	rib height
r_c	concrete radius
s_R	rib spacing
s_r	crack spacing
s_{Rc}	clear rib spacing
u	deformations in x direction
x, r, φ	cylindrical coordinates

Latin upper case

A_c	cross-sectional area of the concrete
A_{gt}	steel strains at the ultimate strength
A_s	cross-sectional area of the steel
E_c	E-Modulus of concrete
E_s	E-Modulus of steel
F	force, applied external load

Special characters

Ø	diameter

Greek lower case

α	inclination of the conical compression field
β	inclination of the contour surface EF
γ	inclination of the nodal zone ABK
δ	slip
ε	strains
η_{cc}	effectiveness factor for concrete subjected to uniaxial compression
η_{ct}	effectiveness factor for concrete subjected to uniaxial tension
σ	normal stresses
σ_c	concrete stresses
σ_s	steel stresses
$\sigma_{s,max}$	maximum steel stresses (at the crack)
τ_b	bond shear stresses
φ	cylindrical coordinate, angle of internal friction

Indices

c	concrete
m	mean
s	steel
u	ultimate limit state
y	yielding

the surrounding concrete at their interface. This highly complex force transfer is commonly modelled using nominal bond shear stresses uniformly distributed around the bar perimeter and varying along the bar axis as a function of either the nominal slip between concrete and steel or the steel stresses [1,4]. This crude idealisation cannot provide a mechanical understanding of the local interface behaviour, but it is commonly used to analyse the load-deformation behaviour by solving the differential equation of bond (derived by Kuuskoski [5] and first solved by Rehm [6]), which presumes that the nominal bond shear stress-slip relationship is known and unique. However, as outlined above, this assumption is strictly speaking mechanically ill-founded, as the behaviour depends as much on the global member configuration as the local interface characteristics. In fact, it has been experimentally shown that the bond shear stress-slip relationship varies considerably even along the short embedded length in standardised pull-out tests [7,8], and that – while it indeed strongly depends on the characteristics of the local interface (e.g. rib geometry [9–11]) – the relationship is strongly affected by the global member configuration, where longitudinal splitting cracks have been found to be particularly detrimental for bond [12].

Moreover, bond shear stress-slip relationships are conventionally determined from pull-out tests based on averaged global measurements (i.e. applied load and nominal slip at the passive bar end), despite that such tests – generating axial compression in the concrete surrounding the reinforcing bar – are not representative of typical reinforced concrete members, where bond causes axial tensile stresses in the concrete between the cracks. This lacuna can be traced back to the difficulty in measuring the local interface behaviour. It can be mitigated by carrying out experiments on more representative specimens, such as RC ties and measuring local steel strains. First such tests were carried out more than a century ago, providing small cavities in the concrete cover to enable access to the reinforcing bars and track the steel deformations [13–15]. Later on, steel strains were measured by means of strain gauges glued onto and inside reinforcing bars [16–19], where the latter method minimises the bias of the interface but is extremely laborious and expensive. Today, such measurements can be carried out efficiently

using state-of-the-art distributed fibre optical sensing (DFOS) on reinforcing bars [20–26]. Nonetheless, the bond shear stress-slip relationships obtained from such measurements are only representative of situations similar to the underlying experiments. While other configurations can be taken into account by semi-empirically calibrating the bond stresses and the bond stress-slip relationships, such approaches do not provide detailed mechanical insight into the force transfer, neither locally at the interface nor globally to the surrounding concrete.

Nonlinear finite element analyses (NLFEA) have also been used to study bond by modelling the reinforcing bar, the surrounding concrete member and their interface. The behaviour of the interface can be modelled, e.g. by using nominal bond shear stresses as outlined above [27], or included in the proper NLFEA in more detailed investigations modelling the actual rib geometry or including interface elements [28,29]. If the input parameters are suitably chosen – typically calibrated on experiments – such analyses yield realistic predictions of the load-deformation behaviour for a specific case under consideration [30–32]. However, parametric studies are required to gain insight into the governing parameters and their effect, which is computationally expensive and questionable if the configuration differs from the one used to calibrate the input parameters. For these reasons, implementing such detailed bond models in NLFEA of entire structures is hardly ever expedient. In these cases, modifying the stress–strain relationship of the reinforcement to account for the relevant effect of bond on a structural level – i.e. tension stiffening – is computationally much more efficient than modelling the interface [33,34].

Stress field models – either simple strut-and-tie models or more refined discontinuous stress fields – are very useful for understanding the force transfer from the local reinforcing bar-concrete interface to the surrounding concrete. Conceptual strut-and-tie models consisting of conical struts and tension hoops (rings), and wedge-shaped nodal zones at the ribs of deformed reinforcing bars were proposed many decades ago [35] to explain the mechanical bond behaviour. These models allow identifying the relevant parameters and, if combined with suitably calibrated strength criteria for the tensile hoops [35–37], can be used to predict the occurrence of longitudinal splitting cracks. Stress field

models can also be used to study the load-deformation behaviour by assigning adequate member stiffnesses and optimising the geometry to minimise complementary energy, i.e. maximise stiffness, where appropriate [38–40]. However, a meaningful assignment of stiffnesses requires realistic concrete dimensions and hence, the existing conceptual strut-and-tie models are of limited use for this purpose. Instead, consistent stress fields according to the lower-bound theorem of plasticity theory – satisfying equilibrium without infringing the yield conditions of the concrete – are required.

This paper presents such a stress field for the fundamental case of a concrete tie reinforced with one deformed steel bar. The proposed discontinuous axisymmetric concrete stress field between two cracks is composed of individual stress fields for each rib, which allows capturing local effects and the global load transfer. The model provides a good understanding of the flow of forces, the governing failure modes, the distribution of bond stresses, and how confinement could affect the force transfer while relying neither on empirical parameters nor on calibrated bond shear stress-slip relationships. More realistic bond stress distributions along the bar axis can be achieved by assigning stiffnesses to the stress field components and requiring interface compatibility, i.e. ensuring contact between the concrete and the reinforcing bar at every rib. To this end, a simplified approach is proposed to estimate the axial and radial concrete deformations at the interface, assuming a linear elastic behaviour of the concrete. The proposed model is validated against experimental results of three RC ties where steel strains were measured quasi-continuously with DFOS and compared to the Swiss Code provisions [41] in terms of average and local bond stresses, crack spacing, the influence of the bar diameter and the occurrence of splitting.

2. Phenomenology of the reinforcing bar-concrete interaction

This section outlines relevant aspects of the reinforcing steel-–concrete interaction in RC members subjected to uniaxial tension, which serve as the foundation for the stress field model derived in Section 3. The typical bond behaviour of structural concrete is discussed in the following for the particular case of an axisymmetric RC tie, which characteristics are shown in Fig. 1. The reinforcing bar of nominal diameter Ø is subjected to uniaxial tension and experiences the highest steel stresses $\sigma_{s,max}$ at the crack, where the concrete is axially stress-free, i.e. $\sigma_c = 0$. With increasing distance from the crack, the axial concrete tensile stresses increase as the load is transferred from the bar to the surrounding concrete. In contrast, the steel stresses and average steel deformations decrease, which is commonly known as the tension stiffening effect. Depending on the crack spacing s_r, the average concrete tensile stresses at the centre between two adjacent cracks, referred to as ideal cross-section, vary between 0.5 and 1.0 times the concrete tensile strength [4].

The governing bond mechanism for very low loads, at initial loading, is chemical adhesion [42]. At increasing load, the elongation of the reinforcing steel exceeds the strain capacity of the concrete, causing nonlinear deformations and discontinuities such as cracks, crushing, and slip between concrete and steel, leaving mechanical interlock at the ribs and friction as the primary load transfer mechanisms while adhesion vanishes [42]. The crack width varies across the concrete cover thickness since the crack width, which at the interface corresponds to the actual slip between reinforcing bar and concrete, includes a contribution of the concrete strains between the cracks (which is commonly included in the nominal slip, see Section 4). The crack width is typically defined at the concrete surface.

In addition to the main cracks, radial splitting cracks and internal conical cracks originating at the rib tips can form, as illustrated in Fig. 1 (also called micro- or secondary cracks). Rehm [6] identified splitting caused by the wedging action of the ribs as one of two main contributors to slip, with concrete crushing at the ribs – caused by the local load transfer – as the second one. The wedging action of deformed bars, acknowledged by numerous authors, e.g. [35,43,44], is often modelled by simple strut-and-tie models with conical compressive struts spreading the transferred load to the surrounding concrete, where they activate axial concrete ties and circumferential tensile hoops [35,36]. Tepfers derived analytical expressions to quantify the resistance of these tensile hoops assuming constant nominal bond stresses along the bar axis. He assumed potentially cracked, linearly elastic or fully plastic concrete tensile hoops and found the resistance of linear elastic tensile rings to be the highest if the internal zone was radially cracked (split) up to a radius of $0.486 \cdot r_c$, with r_c = radius of the concrete cylinder. Schenkel developed stress fields for bond that extended the tensile hoop solutions of Tepfers for plastic and plastic-cracked behaviour [37]. He focused on anchorage and lap splices in RC elements and the case of small concrete cover without investigating the activation of axial tensile forces in the concrete. This is, however, a key component of the stress field presented in the next section.

3. Discontinuous stress field for bond

3.1. Main assumptions and simplifications

The development of the discontinuous stress field model for bond focuses on an axisymmetric crack element, i.e. the part of an RC tie delimited by two adjacent main cracks (see Fig. 1a). The reinforcing bar ribs are modelled in a discrete manner and the load transfer between the reinforcement and the concrete is limited to mechanical interlocking at the ribs. The model assumes that at each rib, a conical compression field forms, which is equilibrated by annular discs acting as tensile hoops and an axial tension field (see Fig. 2). Conceptually, this corresponds to the simple strut-and-tie models for bond proposed many decades ago [35].
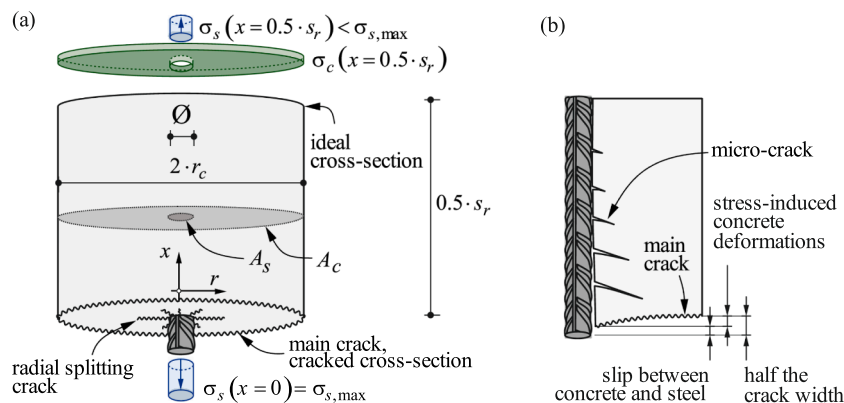

Fig. 1. RC tie characteristics: (a) geometry and stress resultants; (b) deformations over half of the crack spacing s_r.
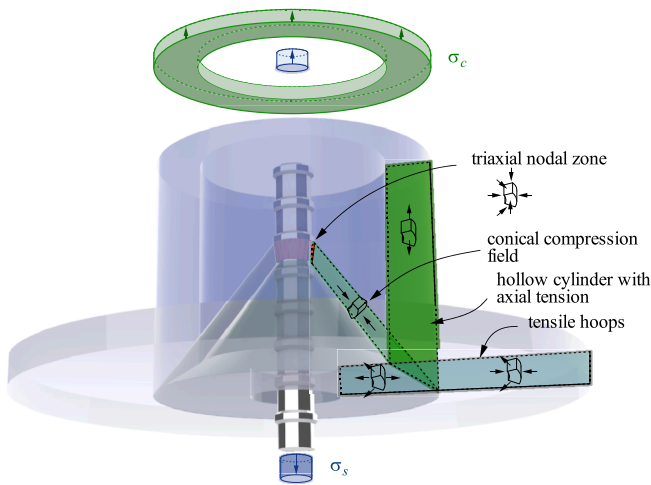
Fig. 2. Proposed stress field originating at one rib of the reinforcing bar.

The detailed formulation of the stress field generated at each rib is inspired by the Dual-Cone stress field developed for partially loaded areas at ETH Zurich [45], particularly concerning the determination of the non-trivial concrete stress states in the vicinity of the rib (triaxial nodal zone) and the conical compression fields.

The geometry of the RC tie is idealised as a concrete cylinder with radius r_c that is reinforced with a concentric reinforcing bar and axisymmetric about the x-axis (i.e. the reinforcing bar axis), as shown in Fig. 1a. Due to symmetry, only half of the crack element is modelled. The ribs are equally spaced at the rib spacing s_R, have a constant rib height h_R, and are inclined by γ_{rib} to the x-axis.

The concrete is idealised as rigid-perfectly plastic in accordance with the theoretical basis of the Theory of Plasticity [44,46] (see uniaxial behaviour in Fig. 3a), i.e. stresses below the plastic compressive and tensile strengths f_c and f_{ct}, respectively, are not inducing deformations. Although reinforced concrete is far from behaving in this way, a rigid-perfectly plastic idealisation results in a safe design when dimensioning and detailing appropriately, i.e.,:avoiding excessively high or low reinforcement ratios, limiting the inclination of compression struts and choosing the material strengths in a suitable manner (i.e. appropriate reduction factors) to account for the limited ductility of the materials. The plastic concrete compressive strength f_c is defined as:

$$f_c = \eta_{cc} \cdot f_{c0} \tag{1}$$

where f_{c0} = uniaxial compressive strength of the concrete and η_{cc} = effectiveness factor accounting for brittleness, softening effects (e.g. due to cracking), size effects, and loading conditions [46,47]. In this study,

where normal-strength concrete is assumed and compression takes place without transverse cracks, $\eta_{cc} = 1.0$ is used. For the tensile strength, the effectiveness factor is needed due to the brittleness of concrete in tension [46]:

$$f_{ct} = \eta_{ct} \cdot f_{ctm} \tag{2}$$

where f_{ctm} = mean tensile strength and factor η_{ct} = effectiveness, with η_{ct} = 0.7 if a uniform tensile stress distribution is assumed (based on the observed maximum concrete tensile stresses reached in the RC ties observed in [48] and findings from [49]), and η_{ct} = 1.0 for a variable stress distribution, i.e. if the tensile strength is reached merely in a single point.

In the proposed stress field, multiaxial stress states occur. This is, for instance, the case of the triaxial nodal zone forming adjacent to the rib or in areas where the conical compression field and the axial tension field intersect (see Fig. 2). A modified Mohr-Coulomb (MC) failure criterion is adopted as a suitable yield condition for such stress states, where the tensile strength is limited to f_{ct} (see Fig. 3b) [50]:

$$Y = \sigma_1(1 + \sin\varphi) - \sigma_3(1 - \sin\varphi) - 2c\cos\varphi \leqslant 0$$
$$\sigma_1 \leqslant f_{ct} \tag{3}$$
$$\sigma_1 \geqslant \sigma_2 \geqslant \sigma_3$$

where φ = angle of internal friction (taken as $\tan\varphi = 3/4$), c = cohesion (taken as $f_c/4$) [46] and σ_1, σ_2 and σ_3 = principal stresses. The compressive strength in uniaxial and plane stress states is given by Eq. (1). For triaxial stress states (plane strain), the triaxial compressive strength results from Eq. (3) as $f_{c3} = \sigma_3 = f_c + 4 \cdot \sigma_1$.

The force applied in the RC tie is selected in the model below the ultimate capacity of the reinforcing bar, guaranteeing that the maximum stress of the reinforcing bar at the crack ($\sigma_{s,max}$) does not exceed its tensile strength (f_{su}). The stresses in the reinforcement between the cracks follow directly from equilibrium once the concrete stress field is defined. The consideration of the influence of the steel deformations on the force transferred between the concrete and the bar will be explored in Section 4.2.

3.2. Conceptual development of the stress field

Fig. 2 illustrates the axisymmetric discontinuous stress field for one rib, which comprises four components whose shape and function are explained in the following before providing the detailed analytical formulation in Section 3.3. Such a stress field is developed consecutively at every rib i, starting from the main crack (see Fig. 4), and the stress fields of all ribs are superimposed to form the overall stress field.

The concentrated load introduced by each rib results in a concrete nodal zone ABK which is a truncated cone with a concentric cylindrical hole subjected to a triaxial stress state. The load transferred by the rib is
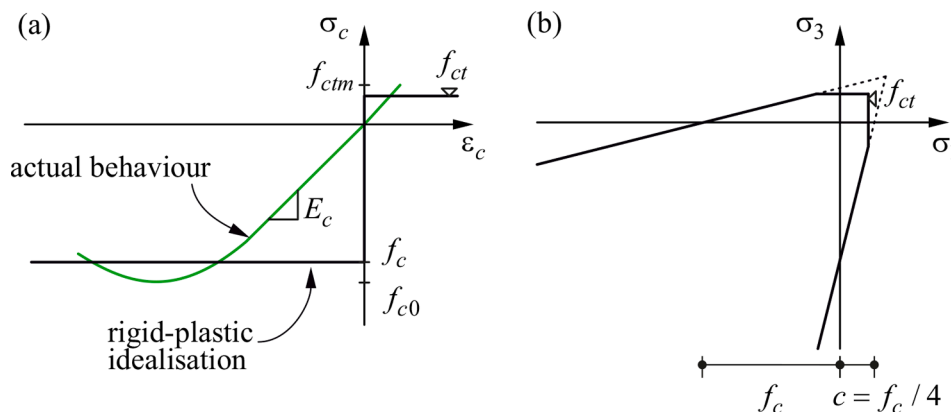

Fig. 3. Concrete constitutive idealisation: (a) actual and modelled constitutive behaviour under uniaxial compression and tension; (b) multiaxial loading failure criterion (plane-strain state).
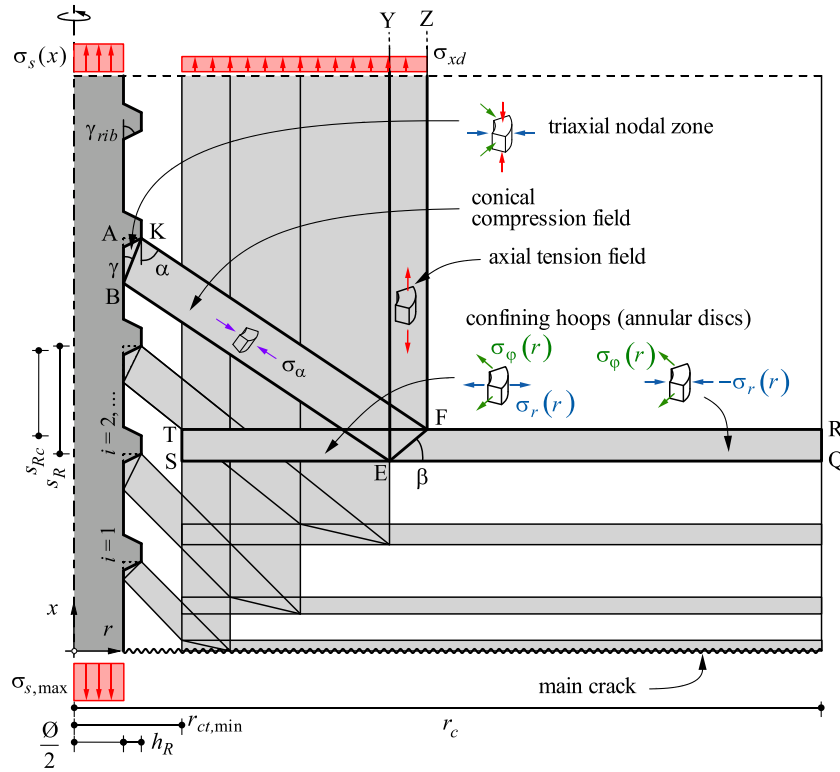
Fig. 4. Progressive development of the axisymmetric stress field until the fourth rib.

composed of axial stresses σ_{x0} acting on the annulus AK and radial stresses σ_{r0} on the cylinder AB. Note that a similar nodal zone was proposed in [44,51] for a case with axial compression in the concrete (which would apply in a pull-out test but not in a tie). The inclination γ to the *x*-axis defines the size of the nodal zone; it can vary between the rib flank inclination $\gamma_{max} = \gamma_{rib}$ (nodal zone vanishes) and $\gamma_{min} = $ atan (h_R/s_{Rc}) (nodal zone intersects adjacent rib), where $s_{Rc} = $ clear rib spacing. The beneficial stress state in the triaxial zone allows the transfer of high, concentrated loads (see Section 3.3.1).

Along its discontinuity surface BK, the triaxial nodal zone is equilibrated by a uniaxial parallel compression field forming a hollow cone (BEFK), which is conically truncated at both ends and hereafter referred to as conical compression field. Its principal direction $\varphi_3 = \alpha$ is generally not perpendicular to the surface BK, and the uniaxial stresses decrease inversely proportional to the radius along their trajectories (see Section 3.3.2). The conical compression field spreads the loads radially to the outer contour surface EF, where they are diverted into axial tension and a radial component carried by annular discs acting as tensile hoops. The contour surface EF is inclined at an angle β to the *r*-axis; note that depending on the configuration, the angle β can be positive (as in the labelled stress field in Fig. 4) or negative (as in the remaining stress fields in the same figure). The inner radius of the contour surface EF (Point E) is defined by the smallest radius at which axial tension can be activated by the rib under consideration, i.e. the outer radius (Point F) of the corresponding contour surface of the precedent rib except for the first rib. For the latter, the minimum radius $r_{ct,min}$ where concrete may carry tension superimposed with conical compression – without this superposition governing failure – is defined in Section 3.3.3. The axial component of the conical compression field is carried along EF by the hollow cylinder (EYZF) and in equilibrium with the corresponding stresses activated on the mirrored (symmetric to the ideal section) side of the crack element. The radial component of the conical compression field is carried along EF by an annular disc loaded along its inner circumference (EQRF) subjected to radial compression (providing conventional confinement) and another annular disc loaded along its outer

circumference (ESTF) subjected to radial tension (providing tensile confinement).

This model can be used to find a suitable stress field for a given distribution of bond stresses along the crack element. However, the present paper focuses on the determination of the local bond stresses, which requires an additional criterion to determine the geometry of the stress field. To this end, the bond force transferred at every rib is maximised. Hence, when developing the stress field at a rib, the three variables that define the stress field of the rib (α, β and γ) are set to maximise the load transfer while fulfilling geometrical boundary conditions without infringing the failure criteria. The development of the stress field progresses to subsequent ribs until the axial tension field reaches the edge of the tie. This location, where the longitudinal tensile capacity of the tie is reached, corresponds to the ideal cross-section and determines the crack spacing s_r.

3.3. Analytical formulation of the stress field

3.3.1. Triaxial stress state in the nodal zone ABK, steel and bond stresses

The stresses acting axially and radially on the nodal zone ABK are related to the uniaxial stress $\sigma_{\alpha0}$ of the conical compression field acting along BK and the angles α and γ. Generally, within ABK, the radial stresses σ_r vary in the *x*-direction and the axial stresses σ_x vary in the *r*-direction due to the assumption of a uniform uniaxial tension field in the hollow cylinder (EYZF), causing non-uniform stresses σ_{x0}, σ_{r0} and $\sigma_{\alpha0}$ along the boundaries of the nodal zone (see Section 3.3.2); the circumferential and radial stresses are assumed to coincide at each point within ABK. Equilibrium can be formulated at each point of the discontinuity surface BK in *x*- and *r*-direction (see Fig. 5a) as follows:

$$\sum F_x \equiv 0 : \sigma_{x0} = \sigma_{\alpha0} \cdot \cos\alpha \cdot \frac{\sin(\alpha + \gamma)}{\sin\gamma} \tag{4}$$

$$\sum F_r \equiv 0 : \sigma_{r0} = \sigma_{\alpha0} \cdot \sin\alpha \cdot \frac{\sin(\alpha + \gamma)}{\cos\gamma} \tag{5}$$
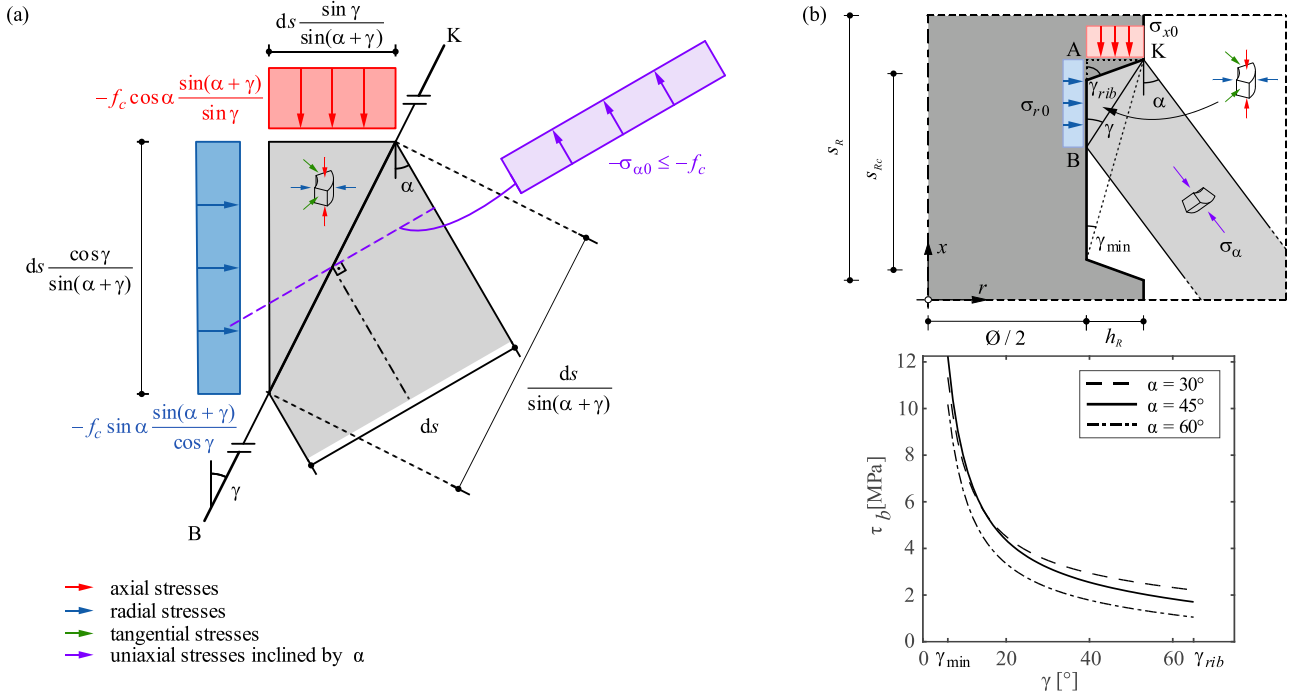
Fig. 5. Nodal zone ABK: (a) equilibrium of the infinitesimal strut of width ds at the discontinuity BK; (b) influence of the variation of α and γ on the load transfer assuming $\sigma_{\alpha 0} = f_c$ (steel and concrete properties set to those of Specimen Ø16.M.ND#2, see Table 1).

The stresses in ABK need to satisfy the failure criterion provided by the yield condition in Eq. (3).

The total bond force, i.e. the transferred axial load $F_{\tau,i}$ at a specific rib i, which defines the force and stress variations in the reinforcing bar, can be calculated by integrating the axial stresses applied at the rib, or by considering vertical equilibrium of the conical compression field BEFK:

$$F_{\tau,i} = -\int_{\emptyset/2}^{\emptyset/2+h_R} \sigma_{x0,i}(r)\cdot 2\pi\cdot r \ \mathrm{d}r = \sigma_{xd}\cdot\pi\cdot\left(r_F^2 - r_E^2\right) \qquad (6)$$

and the nominal bond stresses τ_b over the length of a rib spacing are thus:

$$\tau_b = \frac{F_\tau}{\pi\cdot\emptyset\cdot s_R} \qquad (7)$$

The influence of α and γ on the transferred load are shown in Fig. 5b, where for illustration the uniaxial compressive stresses $\sigma_{\alpha 0}$ along BK have been assumed to be uniform and equal to f_c. It can be observed that the smaller γ, i.e. the bigger the triaxial zone, the higher the bond stresses. The angle α has a minor influence but becomes more significant for large γ. The optimum α changes depending on γ.

3.3.2. Conical compression field BEFK

Equilibrium along EF depends on α and β (Fig. 6). Assuming constant uniaxial stresses $\sigma_{\alpha d}$ along EF and splitting it into its radial and axial components σ_{rd} and σ_{xd}, respectively, one gets:

$$\sum F_x \equiv 0 : \sigma_{\alpha d}\cdot\cos\alpha = -\sigma_{xd}\cdot\frac{\cos\beta}{\cos(\alpha - \beta)} \qquad (8)$$
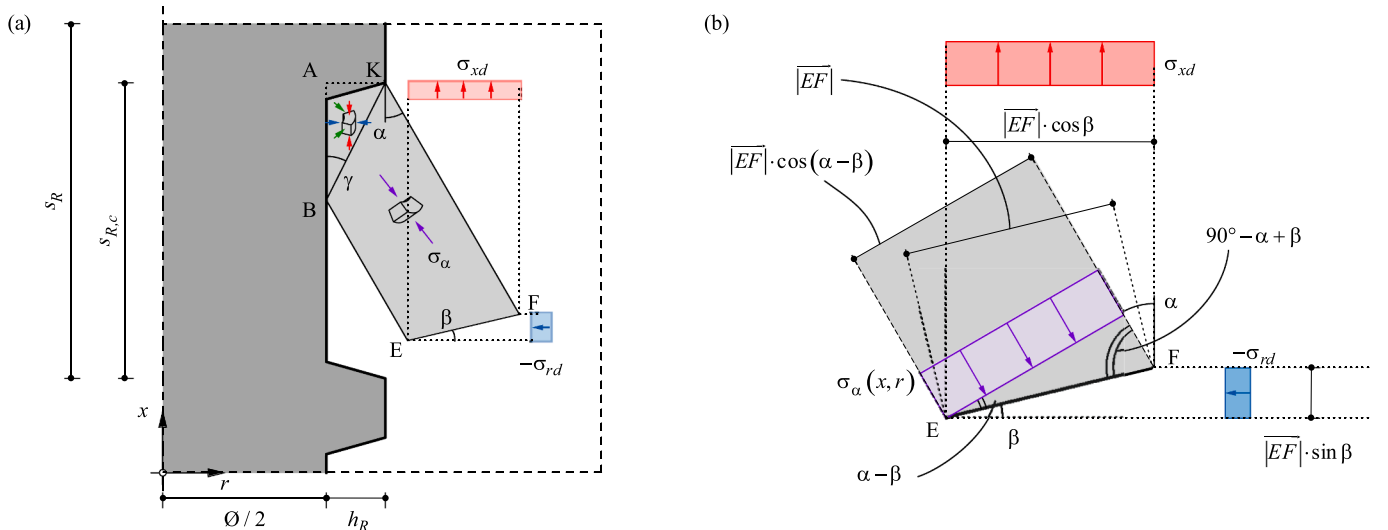

Fig. 6. Conical compression field BEFK: (a) overview and geometry and (b) equilibrium at the discontinuity EF.

$$\sum F_r \equiv 0 : \sigma_{\alpha d}\cdot\sin\alpha = \sigma_{rd}\cdot\frac{\sin|\beta|}{\cos(\alpha-\beta)} \tag{9}$$

Dividing Eq. (9) by Eq. (8) yields the following relation between the radial and axial stresses in EF as a function of the angles α and β:

$$\sigma_{rd} = -\sigma_{xd}\cdot\frac{\tan\alpha}{\tan|\beta|} \tag{10}$$

The constant uniaxial stress $\sigma_{\alpha d}$ along EF implies that this discontinuity is a contour surface of the stress field in BEFK as shown in Fig. 7a, meaning that σ_{rd} and σ_{xd} are also constant along EF, which results in $\sigma_{\alpha 0}$ varying along BK unless it is also a contour surface, which applies only if the extensions of EF and BK intersect the symmetry axis at the same location (all contour surfaces of BEFK are cones with apex at the intersection of EF with the symmetry axis). The uniaxial stresses σ_α in the conical compression field BEFK decrease inversely proportional to the radius along their trajectories for a constant angle of inclination α, and can be expressed depending on the stress $\sigma_{\alpha d}$. To this end, the help variable $\zeta \in [0,1]$ is introduced according to Fig. 7b. The uniaxial stresses σ_α in the conical compression field BEFK in any Point $Q(x,r)$ follow from $\sigma_{\alpha d}$ as:

$$\sigma_\alpha(x,r) = \sigma_{\alpha d}\cdot\frac{r_M(\zeta)}{r} = \sigma_{\alpha d}\cdot\frac{x-x_E+r\cdot\cot\alpha+r_E\cdot\tan\beta}{r\cdot(\tan\beta+\cot\alpha)} \tag{11}$$

where x_M and r_M = coordinates of Point M and $x = x_M + (r_M - r)\cdot\cot\alpha$ (see Fig. 7b). With this and Eq. (8), Eq. (11) becomes:

$$\sigma_\alpha(r,\zeta) = -\frac{\sigma_{xd}}{\cos\alpha}\frac{\cos\beta}{\cos(\alpha-\beta)}\frac{x_M(\zeta)+r_M(\zeta)\cdot\cot\alpha-x_E+r_E\cdot\tan\beta}{r\cdot(\tan\beta+\cot\alpha)} \tag{12}$$

where the coordinates of Point M can be expressed as a function of ζ:

$$r_M = r_E + \zeta\cdot(r_F - r_E) \qquad x_M = x_E + \zeta\cdot(r_F - r_E)\cdot\tan\beta \tag{13}$$

The maximum stresses in the conical compression field BEFK along BK are thus:

$$\sigma_{\alpha 0}(\zeta) = \sigma_{\alpha d}\cdot\frac{r_M(\zeta)}{r_N(\zeta)} = -\frac{\sigma_{xd}}{\cos\alpha}\cdot\frac{\cos\beta}{\cos(\alpha-\beta)}\cdot\frac{x_M(\zeta)+r_M(\zeta)\cdot\cot\alpha-x_E+r_E\cdot\tan\beta}{r_N(\zeta)\cdot(\tan\beta+\cot\alpha)} \tag{14}$$

where x_N and r_N = coordinates of Point N (see Fig. 7b), which can again be expressed as a function of ζ:

$$r_N = r_K - (x_K - x_B)\cdot\tan\gamma + \zeta\cdot h_R = r_B + \zeta\cdot h_R x_N = x_B + \zeta\cdot h_R\cdot\cot\gamma \tag{15}$$

Eqs. (4), (5) and (14) allow determining the axial and radial stresses applied by the rib:

$$\sigma_{x0}(\zeta) = -\frac{\sigma_{xd}}{\cos\alpha}\frac{\cos\beta}{\cos(\alpha-\beta)}\cdot\frac{x_M(\zeta)+r_M(\zeta)\cdot\cot\alpha-x_E+r_E\cdot\tan\beta}{r_N(\zeta)\cdot(\tan\beta+\cot\alpha)}\cdot\cos\alpha\cdot\frac{\sin(\alpha+\gamma)}{\sin\gamma} \tag{16}$$

$$\sigma_{r0}(\zeta) = -\frac{\sigma_{xd}}{\cos\alpha}\frac{\cos\beta}{\cos(\alpha-\beta)}\cdot\frac{x_M(\zeta)+r_M(\zeta)\cdot\cot\alpha-x_E+r_E\cdot\tan\beta}{r_N(\zeta)\cdot(\tan\beta+\cot\alpha)}\cdot\sin\alpha\cdot\frac{\sin(\alpha+\gamma)}{\cos\gamma} \tag{17}$$

The annular discs acting as hoops carry the radial stresses σ_{rd} (see Section 3.3.4) and the axial stresses σ_{xd} activate the concrete in tension inside a hollow cylinder extending from EF to the ideal cross-section (see Section 3.3.3). The axial tensile stresses σ_{xd} are set equal to the plastic concrete tensile strength:

$$\sigma_{xd} \equiv f_{ct} = \eta_{ct}\cdot f_{ctm}(\eta_{ct} = 0.7) \tag{18}$$

3.3.3. Axial tension field

As already introduced in the previous section, uniform axial tensile stresses corresponding to the plastic capacity ($\sigma_{xd} = f_{ct}$) are assumed in the hollow cylinders of the axial tension field. This consideration simplifies the model but implies that the tie always fails by reaching its axial tensile capacity, which generally does not result in the maximum bond capacity. The impact of this assumption is discussed in Section 4, where an alternative procedure to capture cases where the failure of the concrete tensile hoops becomes governing is presented.

The axial tension field generated by a specific rib intersects the conical compression fields of the subsequent ribs. Hence, both stress fields would need to be superimposed in order to verify the yield criterion. The model assumes that the inner part of the tie carries no tensile stresses over a radius $r_{ct,\text{min}}$, such that the region where the stress fields intersect is not governing and hence, the conical compression field can be verified only by checking that its maximum stress (at the boundary BK of the triaxial nodal zone) is below its uniaxial compressive strength. Details of the superposition of the stress fields are given in Appendix A. As a result, the inner radius of the axial tensile hollow cylinder activated by the first rib is set equal to:

$$r_{ct,\text{min}} = \frac{f_c}{f_{c,red}}\cdot\left(\frac{\emptyset}{2}+h_R\right) \approx 1.5\cdot\left(\frac{\emptyset}{2}+h_R\right) \tag{19}$$
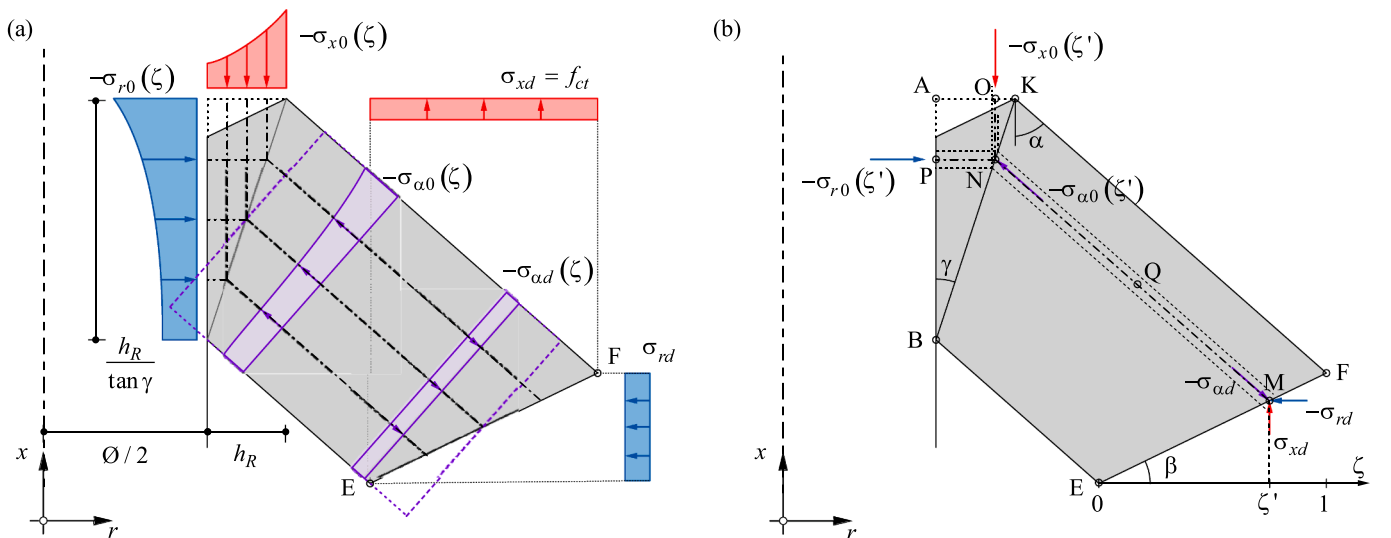

Fig. 7. Stress distributions in ABK and BEFK: (a) stress distributions for an assumed distribution $\sigma_{xd} = f_{ct}$; (b) determination of stresses in an infinitesimal strut as a function of variable $\zeta \in [0,1]$.

3.3.4. Annular discs acting as concrete tensile hoops

The radial component of the conical compression field BEFK is equilibrated along the discontinuity EF by two annular discs: (a) an inner one (ESTF) loaded with radial tension $\sigma_{rd,ID}$ along its outer circumference and (b) an outer one (EQRF) loaded with radial compression $\sigma_{rd,OD}$ along its inner circumference ($(\sigma_{rd}) = \sigma_{rd,ID} + \varepsilon\sigma_{rd,OD}$)). Both annular discs are subjected to tangential tension (σ_φ) and radial tension or compression (σ_r). The inner radius of the inner annular disc ($r_{i,ID} = r_{ct,min}$) and the outer radius of the outer annular disc ($r_{o,OD} = r_c$) are constant. The radii defining the boundary between the inner and the outer annular disc ($r_{o,ID} = r_{i,OD}$) vary slightly along the discontinuity EF (see Fig. 4). For the verification, the average radius is considered.

Several statically admissible stress solutions exist for a radially loaded annular disc. In this study, the tangential stresses (σ_φ) are assumed to be constant (see Fig. 8), resulting in:

$$\sigma_{\varphi,ID} = \sigma_{rd,ID} \cdot \frac{r_{o,ID}}{r_{o,ID} - r_{i,ID}} \tag{20}$$

$$\sigma_{\varphi,OD} = -\sigma_{rd,OD} \cdot \frac{r_{i,OD}}{r_{o,OD} - r_{i,OD}} \tag{21}$$

The distribution of the applied radial load between the inner and the outer disk can be freely chosen as long as the tensile stresses given in Eqs. (20) and (21) do not exceed the concrete tensile capacity defined by Eq. (2) (note that for the tangential stresses $\eta_{ct} = 0.7$ applies, while $\eta_{ct} = 1.0$ is to be used for the radial stress in the inner annular disc). If the radial tension of the inner annular disc is not governing (which is the case in the following examples), the radial stresses are split between both annular discs such that the tangential stresses in the inner and the outer disc are equal ($\sigma_{\varphi,ID} = \sigma_{\varphi,OD} = \sigma_\varphi$).

The model could include the contribution of transverse reinforcement (e.g. transverse stirrups or fibre-reinforced concrete) to capture the corresponding enhancement of bond due to the additional confinement. However, while the bursting force resisted by the confining reinforcement could essentially be modelled as in the Dual-Cone stress field for partial area loading [45], modelling of the confining action in the uncracked state is not straightforward, since at low radial deformations, the stresses in the confining reinforcement may be considerably below the yield stress.

3.4. Numerical solution process

The main equations and assumptions of the model are summarised in Fig. 9. The stress field model comprises the equilibrium equations, geometrical boundary conditions, and the yield conditions of the materials. The analytical model, which has been implemented in Matlab, is consecutively solved at every rib, starting from the rib adjacent to the main crack (where the steel stress is known), until the total axial tensile capacity is reached. The geometry of the stress field at each rib is defined by the variables α, β and γ, which are varied at a discrete step size. Initially, all admissible solutions at the rib are determined. From this set of admissible $\{\alpha, \beta, \gamma\}$-combinations, the solution with the highest bond force transfer is selected as the optimum. Finally, the steel stress in the successive rib is determined, and the process is repeated until the ideal cross-section has been reached or the total force applied to the tie has been anchored (if the applied force is below the cracking load of the tie). The resulting stress fields are independent of the applied load (even if the reinforcing bar yields) as long as it is equal to or higher than the cracking load.

3.5. Results and discussion

The stress field is used to model the behaviour of a series of concrete tie experiments conducted by the authors [48]. The experiments were instrumented with distributed fibre optical sensing (DFOS), which provided distributed steel strain measurements from which local results of bond and slip were calculated. Three concrete ties with a length of 1360 mm (first tie) and 1500 mm (remaining two ties), respectively, reinforced with normal-strength cold-worked deformed steel bars of diameter 14, 16 and 20 mm are discussed in the following, namely specimens Ø14.U.ND#3, Ø16.M.ND#2 and Ø20.M.ND#1 [48]. As these specimens had a square cross-section of 150×150 mm^2, a circular section with an equivalent radius $r_{c,eq} = 84.6$ mm of equal cross-sectional area is considered in the stress field model. In this way, the tensile capacity of the concrete cross-section is well-modelled, but the confinement of the concrete cover might be overpredicted. The material and geometrical properties of the reinforcing steel and concrete are summarised in Table 1. For the model validation, the model results are compared to the experimental data corresponding to the load step with the highest average bond stresses, for all crack elements of each tie (6…12 depending on the specimen). The results are further compared to the
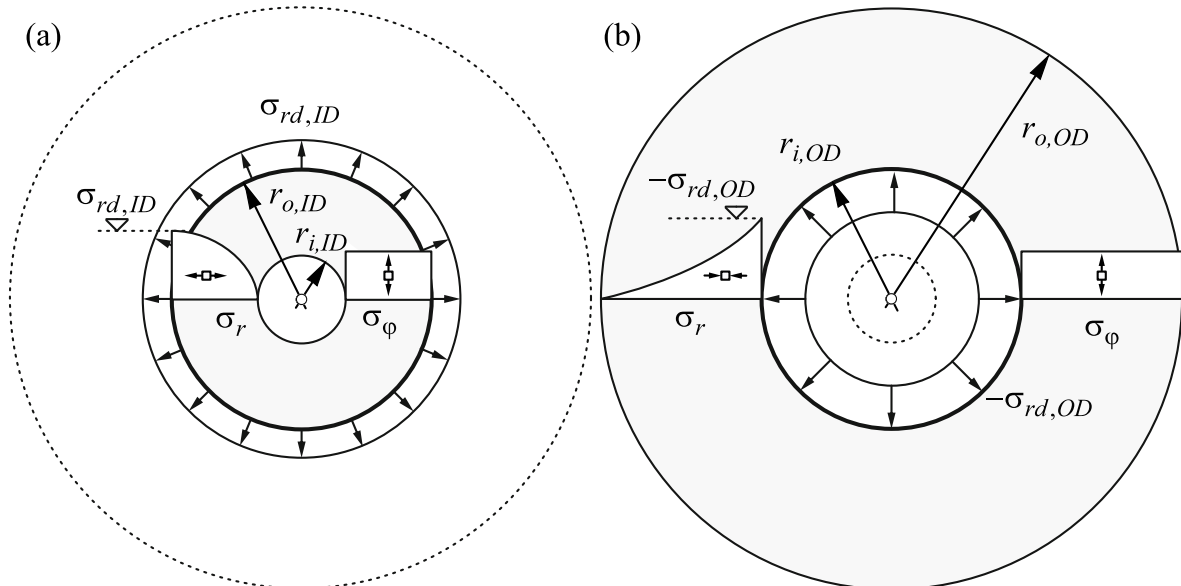

Fig. 8. Assumed stress field for the concrete tensile hoops formed by two annular discs with (a) external and (b) internal radial loading.
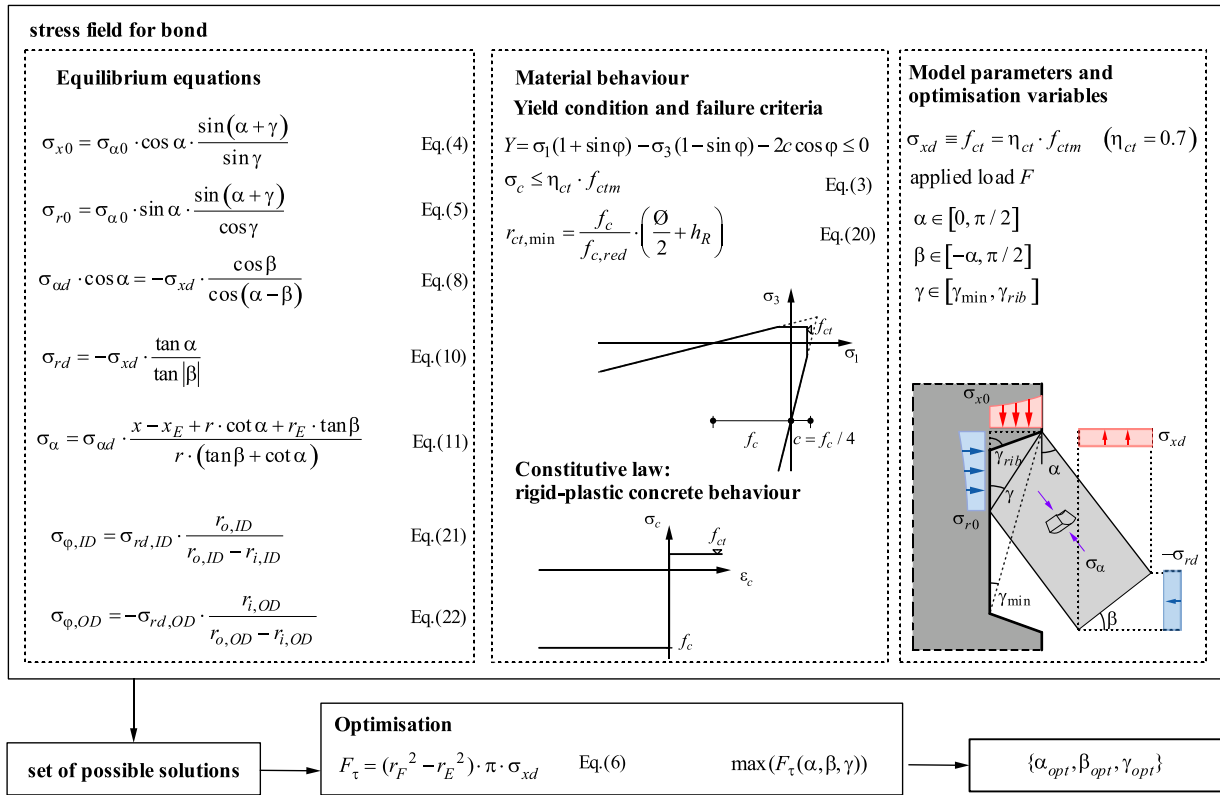
stress field for bond

Equilibrium equations

$$\sigma_{x0} = \sigma_{\alpha 0} \cdot \cos\alpha \cdot \frac{\sin(\alpha + \gamma)}{\sin\gamma} \qquad \text{Eq.(4)}$$

$$\sigma_{r0} = \sigma_{\alpha 0} \cdot \sin\alpha \cdot \frac{\sin(\alpha + \gamma)}{\cos\gamma} \qquad \text{Eq.(5)}$$

$$\sigma_{\alpha d} \cdot \cos\alpha = -\sigma_{xd} \cdot \frac{\cos\beta}{\cos(\alpha - \beta)} \qquad \text{Eq.(8)}$$

$$\sigma_{rd} = -\sigma_{xd} \cdot \frac{\tan\alpha}{\tan|\beta|} \qquad \text{Eq.(10)}$$

$$\sigma_\alpha = \sigma_{\alpha d} \cdot \frac{x - x_E + r \cdot \cot\alpha + r_E \cdot \tan\beta}{r \cdot (\tan\beta + \cot\alpha)} \qquad \text{Eq.(11)}$$

$$\sigma_{\varphi, ID} = \sigma_{rd, ID} \cdot \frac{r_{o, ID}}{r_{o, ID} - r_{i, ID}} \qquad \text{Eq.(21)}$$

$$\sigma_{\varphi, OD} = -\sigma_{rd, OD} \cdot \frac{r_{i, OD}}{r_{o, OD} - r_{i, OD}} \qquad \text{Eq.(22)}$$

Material behaviour
Yield condition and failure criteria

$$Y = \sigma_1(1 + \sin\varphi) - \sigma_3(1 - \sin\varphi) - 2c\cos\varphi \le 0$$

$$\sigma_c \le \eta_{ct} \cdot f_{ctm} \qquad \text{Eq.(3)}$$

$$r_{ct,\min} = \frac{f_c}{f_{c,red}} \cdot \left(\frac{\varnothing}{2} + h_R\right) \qquad \text{Eq.(20)}$$

Constitutive law:
rigid-plastic concrete behaviour

Model parameters and optimisation variables

$$\sigma_{xd} \equiv f_{ct} = \eta_{ct} \cdot f_{ctm} \qquad (\eta_{ct} = 0.7)$$

applied load F

$$\alpha \in [0, \pi/2]$$
$$\beta \in [-\alpha, \pi/2]$$
$$\gamma \in [\gamma_{\min}, \gamma_{rib}]$$

set of possible solutions

Optimisation

$$F_\tau = (r_F{}^2 - r_E{}^2) \cdot \pi \cdot \sigma_{xd} \qquad \text{Eq.(6)} \qquad \max(F_\tau(\alpha, \beta, \gamma))$$

$$\{\alpha_{opt}, \beta_{opt}, \gamma_{opt}\}$$

Fig. 9. Schematic overview of the model components: discontinuous stress field with varying α, β, γ and failure criteria.

Table 1
Material and geometrical properties of the RC ties from [48] used for validating the stress field.

specimen	Ø [mm]	f_{sy} [MPa]	f_{su} [MPa]	E_s [GPa]	ε_{su} [‰]	A_{gt} [‰]	$h_{R,max}$ [mm]	h_R [mm]	s_R [mm]	f_R [%]	γ_{rib} [°]	f_c [MPa]	f_{ct} [MPa]	E_c [GPa]
Ø14.U.ND#3	14	517	621	192.3	112	78	1.4	0.9	6.5	14.7	40	36.1	2.94	30.3
Ø16.M.ND#2	16	540	611	198.5	68	49	1	0.6	9	8.5	65	33.6	3.20	29.1
Ø20.M.ND#1	20	505	581	197.0	97	60	1.2	0.9	12	7.7	39	36.1	2.94	30.3

predictions by the Swiss Standard SIA 262:2013 [41], which is based on the Tension Chord Model (TCM) [4]. The TCM allows analytically solving the differential equation of bond [5], assuming a stepped rigid-plastic bond shear stress distribution with bond stresses $\tau_{b0} = 2 \cdot f_{ctm}$ and $\tau_{b1} = f_{ctm}$ for elastic and plastic steel stresses, respectively, independent of the nominal slip.

The resulting stress fields are shown in Fig. 10a. The solutions are representative of any load within the cracked elastic range of the RC ties. The stress field is represented twice: on the left side, the conical compression field is plotted on the front, while the right side focuses on the annular discs acting as hoops. For the first three ribs, the inclination of the compression field α was limited to 45° based on experimental observations of internal micro-cracking of RC ties and shear keys [47,52]. The resulting inclinations of the remaining ribs are between 38° to 58°. In all cases, the optimal values of β are negative for the ribs near the crack, while positive values result further away. All resulting stress fields have some minor local discontinuities which are caused by (i) the step size of 1° used to vary the geometrical variables and (ii) the change in regimes, e.g. the change from negative to positive β: the uniaxial compressive strength at the boundary BK of the triaxial node becomes governing at a certain radius r_E for all admissible negative inclinations β. Hence, only solutions with a positive β remain possible, which results in a pronounced drop of the local bond capacity (see Fig. 10f). This discontinuity can be explained by the fact that no smooth transition from negative to positive inclinations β is possible, since around β = 0 the

annular discs providing confinement are axially very thin, such that all admissible solutions have a pronounced negative or positive inclination β. If no solution with negative β is admissible since the compressive stress along BK is governing, β thus jumps from a negative to a positive value. The associated drop in the bond force is due to the much higher capacity of conical compression fields with a negative inclination β, as these activate thicker-walled hollow cylinders in axial tension (see, e.g. Fig. 4), with both the cylinder wall thickness (and thus the total transferred load) as well as the thickness of the annular discs (and thus the confinement) increasing as β takes on a more negative value. On the contrary, for positive admissible inclinations β much thinner-walled hollow cylinders can be activated (for the same α and γ) and, more importantly, at relatively small positive inclinations β, where the cylinder wall thickness (and thus the total transferred load) would still be relatively large, the confining discs are axially thin (hence provide limited confinement) as mentioned above.

Fig. 10b and c illustrate the resulting local bond stresses and average concrete tensile stresses (integral of bond stresses divided by the concrete cross-sectional area) of the rigid-plastic stress field (SF) and compares them to experimental data (EXP) and the Tension Chord Model (TCM). The variation of the experimental results of all crack elements within each tie highlights the inherent scatter. It can be observed that the stress field is capable of reproducing the increase of the bond stresses near the crack. This build-up of bond is primarily linked to geometry: the available concrete volume (required for the load transfer) increases with
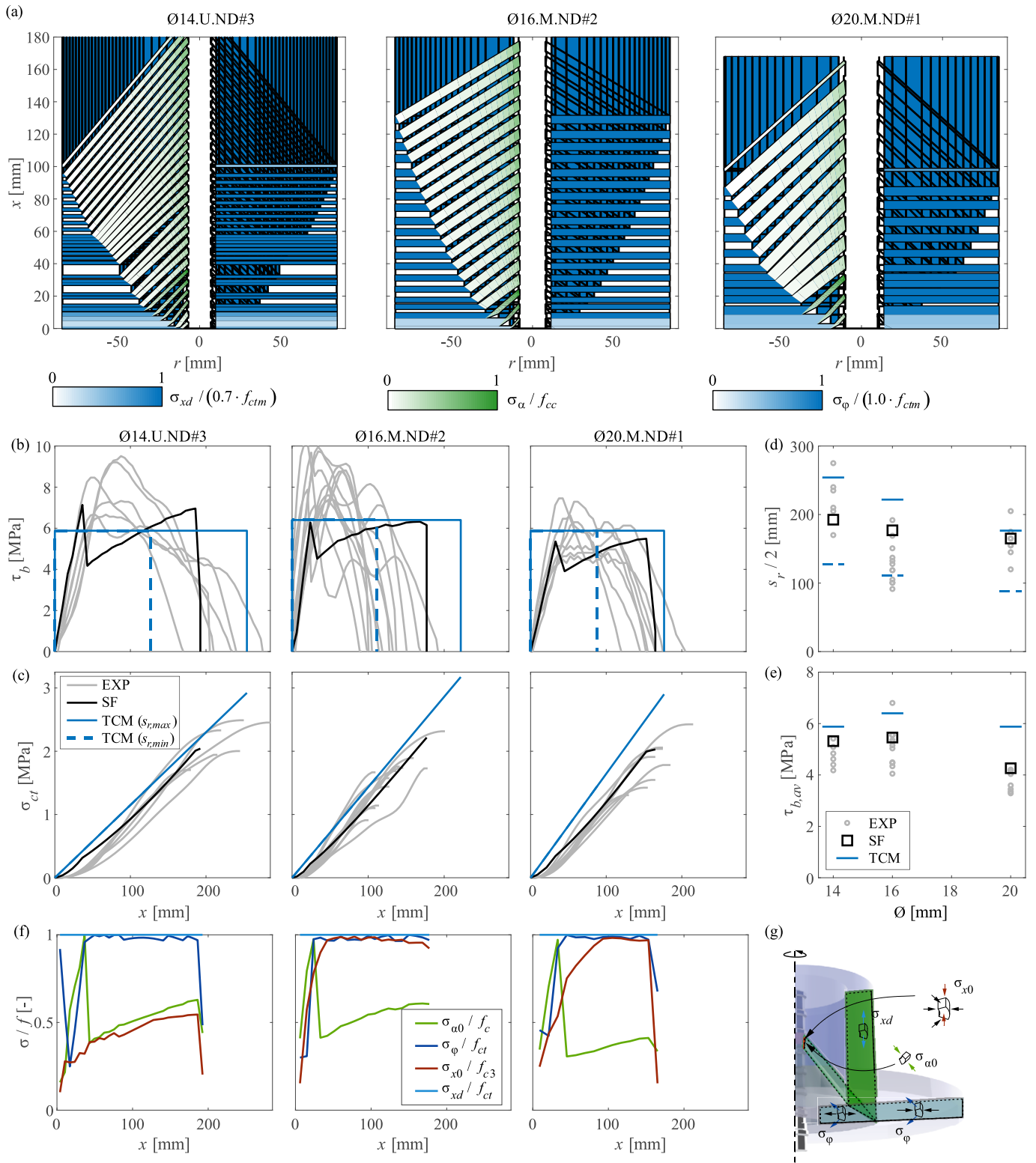
Fig. 10. Results of the stress field model for the RC ties of various bar diameters defined in Table 1: (a) stress fields with highlighted conical compression fields (left) and tensile annular discs (right); (b) bond stress distributions; (c) average axial concrete stress distributions; (d) crack spacings; (e) maximum average bond stresses (experimental data (EXP), stress field (SF), and Tension Chord Model (TCM) [4]); (f) stresses in the stress field compared to corresponding strengths (governing stresses); (g) graphic legend of the stresses shown in (f).

the distance from the crack. The experimentally observed bond stresses decrease progressively after reaching the peak at $x \approx r_c$. Neither the peak nor the subsequent decreasing branch could be accurately predicted with the stress fields. The systematically lower peak bond stresses are

caused by the conical compression fields locally reaching their capacity, which does not correspond with the experimental results. Modelling solutions to address the latter disagreement are discussed in Section 4.1.

The limitations in capturing the local bond behaviour are, however,

not reflected in the global behaviour. The concrete tensile stresses match the experimental data quite well and better than the TCM. The crack spacing (s_r) and average bond stress ($\tau_{b,av}$) can also be reproduced reasonably well (Fig. 10d and e). Furthermore, the stress field captures the trend of smaller crack spacing and lower average bond strength with increasing bar diameter (NB Ø16.M.ND#2 had a higher concrete tensile strength than the other specimens). The TCM is capable of modelling the former effect, but not the latter. Although the average bond stresses derived with the stress field are rather in the upper range of the experimental values, they are still more accurate than the values assumed in the TCM. While the TCM provides excellent minimum and maximum crack spacing predictions, it overestimates the bond strength of these unconfined RC ties, particularly for the case of large diameters (or a high reinforcement ratio, respectively).

4. Exploration of possible model extensions

The stress field presented in Section 3 has the potential to adequately reproduce average bond strengths and maximum crack spacings while accounting for geometrical parameters such as the concrete cover, the bar radius, the rib height and rib spacing. However, one main limitation of the model is the assumption that the axial tensile stresses σ_{xd} activated by each rib are set equal to the plastic concrete tensile strength, which has been observed to yield unrealistically low predictions of the local bond when the maximum capacity of the conical compression field with $\beta < 0°$ is governing. Another limitation is that the model cannot capture phenomena related to concrete and steel deformations, such as the reduced bond strength at large (inelastic) reinforcement strains and the descending branch in the bond stress distribution, see Fig. 10b.

These model limitations are addressed in the following by two modifications (see Fig. 11). In Section 4.1, the axial tensile stresses σ_{xd} activated by each rib are reduced in order to avoid failures of the conical compression field and find solutions with negative inclinations β leading to higher bond stresses. In Section 4.2, stiffnesses are assigned to the

reinforcing bar and the concrete and a simplified interface compatibility condition is introduced, such that the load and steel deformation dependencies of bond can be captured by the model.

4.1. Reduced axial tensile stresses

In Section 3.5, it was shown that local bond may decrease pronouncedly if the uniaxial compressive strength in the conical compression field becomes governing, which does not reflect the experimentally observed behaviour. In such cases, a more realistic stress field can be developed by reducing the axial concrete tensile stress activated by the corresponding ribs to a value below the concrete tensile strength ($\sigma_{xd,i} \le f_{ct}$). This extension of the solution space of admissible stress fields is examined for the 7th rib of Specimen Ø14.U.ND#3 (see Fig. 10a). The bond stresses corresponding to a utilisation of $\sigma_{xd,i} = f_{ct}/3$, $\sigma_{xd,I} = f_{ct}/2$ and $\sigma_{xd,i} = f_{ct}$ in the axial hollow cylinder are shown in Fig. 12a-c, with the angle γ set to its minimum admissible value. The original solution space (Fig. 12a) is enhanced by the reduction of the axial tensile stress to 50% and 33% of the tensile strength (Fig. 12b and c, respectively), providing feasible solutions with larger bond strength, i.e. solutions with $\beta < 0°$. However, this measure affects the successive ribs as the hollow cylinder becomes thicker, reducing the remaining space for the hollow cylinders activated by successive ribs.

The application of the extended model, where not all ribs necessarily activate the full axial tensile capacity of the concrete (i.e. $\sigma_{xd,i} \le f_{ct}$), is explored hereafter. To utilise the capacity of the concrete in axial tension, the r-coordinate of Point E corresponding to Rib $i + 1$ is set equal to that of Point E of the preceding Rib i ($r_{E,i+1} = r_{E,i}$) if Rib i does not activate the full axial tensile strength ($\sigma_{xd,i} \le f_{ct}$). The hollow cylinders activated by subsequent ribs may thus overlap. Generally, the axial tensile capacity of the concrete is fully exploited ($\sum \sigma_{xd,i} = f_{ct}$); the total axial tensile stress is however locally reduced ($\sum \sigma_{xd,i} < f_{ct}$) in case the conical compression field becomes decisive and bond stresses would otherwise decrease abruptly. Fig. 13a illustrates the resulting stress field
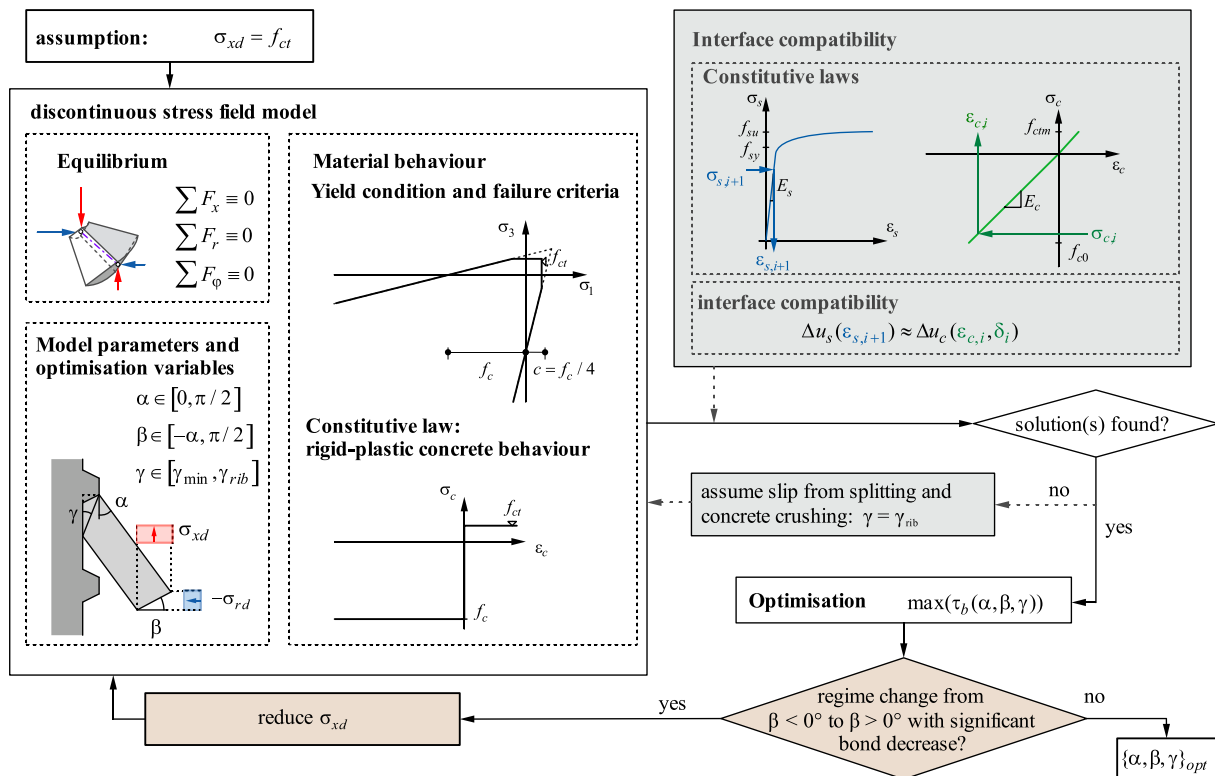

Fig. 11. Schematic overview of the discontinuous stress field model including two main extensions: (i) adjustment of the axial concrete tensile stresses σ_{xd} in case of a regime change from negative to positive β with a significant bond decrease (brown, Section 4.1), and (ii) interface compatibility (grey, Section 4.2).
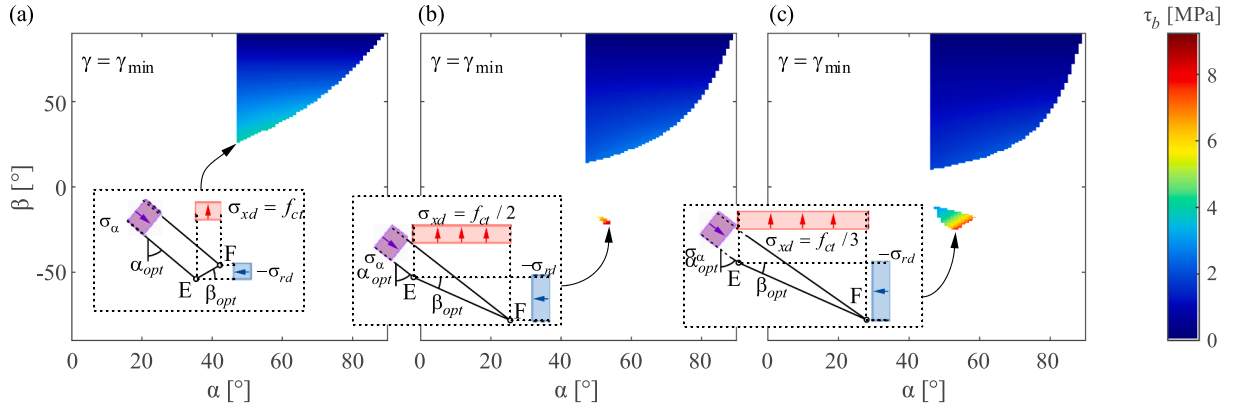
Fig. 12. Resulting bond stresses in the admissible solution space at the 7th rib of Specimen Ø14.U.ND#3 for γ_{min} and corresponding optimal stress field geometry at EF: (a) $\sigma_{xd,i} = f_{ct}$; (b) $\sigma_{xd,i} = f_{ct}/2$; (c) $\sigma_{xd,i} = f_{ct}/3$.
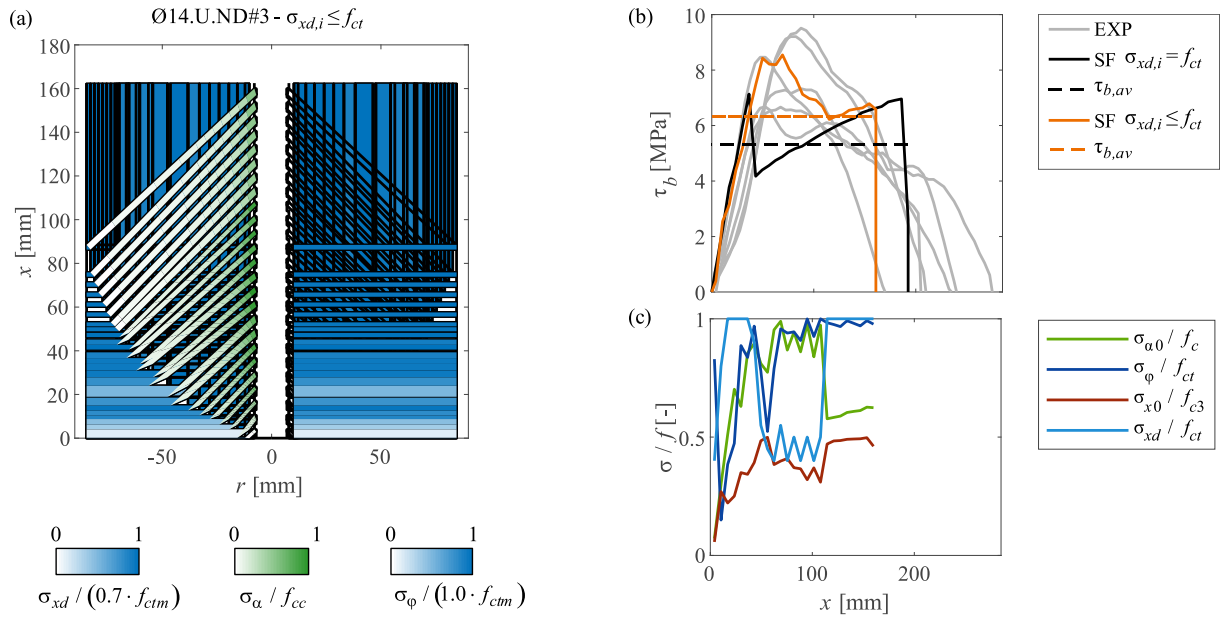

Fig. 13. Stress field development for Specimen Ø14.U.ND#3 with $\sigma_{xd,i} \leq f_{ct}$: (a) stress field topology; (b) bond stress distribution compared to the stress field solution with $\sigma_{xd,i} = f_{ct}$ and experimental data; (c) governing stresses.

for Specimen Ø14.U.ND#3, where the axial tensile stress was reduced at the respective ribs until a feasible solution with $\beta < 0°$ was found. As a reference, for the 8th rib, $\sigma_{xd,8}$ was set to $0.5 \cdot f_{ct}$, and the 9th rib utilised the remaining capacity of the hollow cylinder. A reduction of the axial tensile stress ($\sigma_{xd,i} < f_{ct}$) was applied from the 8th to the 15th rib.

Fig. 13b compares the resulting bond stress distribution (orange) to that of the stress field assuming $\sigma_{xd,i} = f_{ct}$ (black) and experimental data (grey). The stress field with $\sigma_{xd,i} \leq f_{ct}$ captures higher and more realistic bond stress values than when assuming $\sigma_{xd,i} = f_{ct}$. The more efficient solutions with $\beta < 0°$ found with $\sigma_{xd,i} \leq f_{ct}$ are also reflected in the much higher utilisation of the uniaxial compressive strength in the conical compression fields (Fig. 13c, compare to Fig. 10f).

The chosen value of $\sigma_{xd,i}$ highly affects the solution space of the subsequent rib $i + 1$. Hence, a simple maximisation of the transferred load at each rib (starting at the main crack and proceeding towards the ideal section) by optimising $\sigma_{xd,i}$ would yield unrealistic results with a strongly jagged bond stress distribution: the bond force at a specific rib could be maximised with low axial tensile stresses and very flat conical compression fields (large angle α), which would however strongly impair the possible geometries and bond strengths of the compression fields in the following ribs. Such issues were circumvented in the stress

field shown in Fig. 13b by limiting the inclination α of the 6th conical compression field, which caused a slight decrease of the bond stresses at the 6th rib but enabled much higher bond forces at the 7th rib even without reducing $\sigma_{xd,7}$ (see black and orange curve in Fig. 13b before the bond stress drops). This somewhat arbitrary choice, similar to the manual selection of $\sigma_{xd,i} < f_{ct}$, highlights that despite that optimising $\sigma_{xd,i}$ appears to be promising, further work would be required to find an objective optimisation approach that automatically develops meaningful stress fields. This is however beyond the scope of this paper.

4.2. Compatibility at the reinforcing bar-concrete interface

The rigid-plastic stress fields developed in the previous sections aim at maximising the force transfer at each rib for the given configuration without considering deformations, hence they disregard compatibility. While this can be justified based on the lower bound theorem of plasticity theory, the results are of limited use for load-deformation analyses and serviceability considerations such as estimating crack widths. Furthermore, the rigid-plastic stress fields cannot capture the well-known, experimentally substantiated strong impact of high steel deformations: bond stresses decrease significantly at large steel strains, i.e.

when the reinforcement yields. This is reflected in established models such as the TCM, where the bond stresses are reduced to half of the initial value once the reinforcement yields [4].

These shortcomings of the rigid-plastic stress fields are addressed in the following by assigning stiffnesses to the reinforcing bar and the concrete and introducing a simplified compatibility condition requiring contact between the concrete and the reinforcing bar at every rib. Note that unlike compatibility-based stress fields [33] or more general nonlinear finite element analyses, these simple model extensions – in the following referred to as *interface compatibility* – do not ensure a continuous compatible stress field satisfying the stress–strain relationship at each point, as is evident when considering the stress discontinuities at the conical boundaries of the conical compression field. However, the model with interface compatibility maintains the clear mechanical meaning of all components as in the rigid-plastic stress field, and despite being a crude idealisation – essentially corresponding to a Level 2 approximation according to [53] – enables a more realistic consideration of the force transfer between reinforcing bars and surrounding concrete and facilitates carrying out approximate load-deformation analyses.

4.2.1. Main assumptions for interface compatibility

Fig. 11 illustrates the workflow in the development of the stress field considering interface compatibility, which is based on the rigid-plastic stress field presented in Section 3 and adopts the use of reduced axial tensile stresses introduced in Section 4.1. For all admissible rigid-plastic stress fields evaluated according to these previous sections, the steel and concrete deformations and deformation increments at the interface are estimated as further outlined below, discarding solutions where the axial steel deformations and concrete displacements at the interface differ by more than a specified threshold (tolerance). From the remaining set of admissible solutions, the stress field with the highest bond stress is chosen.

The reinforcing bar is assigned a suitable stress–strain relationship. In this study, the relationship proposed by Ramberg-Osgood [54] for cold-worked reinforcing bars is used, as it represents well the constitutive behaviour of the reinforcement in the experiments used for validating the model [48]. The steel displacements consist of the elongation of the reinforcing bar, corresponding to the integral of steel strains from the ideal section to the rib under consideration. In the model, these displacements are determined rib-wise, with Rib i contributing

$$\Delta u_{s,i} = \varepsilon_{s,i+1} \cdot s_R \tag{22}$$

where $\varepsilon_{s,i+1}$ = steel strains between Rib i and $i + 1$ obtained from the steel stresses (which are constant between the ribs) and the stress–strain relationship of the reinforcing bar. The total steel displacement at Rib i then corresponds to the sum of the contributions of all ribs between Rib i and the ideal cross-section.

The concrete in the conical compression field and in the axial tensile hollow cylinders is modelled as linearly elastic in tension and compression, which is a reasonable approximation since high concrete stresses occur only within a short length along the conical compression fields. On the other hand, the deformations of the annular discs acting as hoops are neglected (i.e. the radial coordinates of the points E and F of the rigid-plastic stress field are maintained) since the stresses and deformations of these discs are subject to considerable uncertainty (load sharing of inner and outer annular disc, internal splitting and conical micro-cracks in inner part of the tie $r < r_{ct,min}$, see Fig. 1b and Section 3.3.3). The small deformations of the triaxial nodal zone ABK are also neglected, as well as the contribution of conical micro-cracks (see Fig. 1b) caused by the discontinuity between the conical compression fields (which close to the ribs are subjected to high compressive stresses) and the surrounding stress-free concrete.

Hence, the deformations of the concrete components of the stress fields of each rib consist of the superposition of (i) an axial elongation

due to the tensile strains in the hollow cylinders (see Fig. 14a), with Rib i contributing approximately

$$\Delta u_{ct,i} = (x_K - x_M + s_R) \cdot \frac{f_{ct}}{E_c} \tag{23}$$

where $x_K - x_M + s_R$ = axial distance between Point M of the rib under consideration (see Fig. 7b) and Point K of the subsequent rib, and (ii) a contraction of the conical compression field along its generatrices, with the contour surface EF remaining in place. The contraction of the conical compression field (ii) causes axial concrete displacements at Rib i (Fig. 14b):

$$\Delta u_{cc,i}(\zeta) = \int_{r_N}^{r_M} \sigma_\alpha(\zeta, r) \, \mathrm{d}r \cdot \frac{\cos\alpha}{E_c}$$
$$= \log\left(\frac{r_M(\zeta)}{r_M(\zeta)}\right) \cdot \sigma_{\alpha d} \frac{x_M(\zeta) + r_M(\zeta) \cdot \cot\alpha - x_E + r_E \cdot \tan\beta}{r \cdot (\tan\beta + \cot\alpha)} \cdot \frac{\cos\alpha}{E_c} \tag{24}$$

with r_M and r_N radial coordinates of Points M and N according to Eqs. (13) and (15), respectively (see also Fig. 7b), as well as radial concrete displacements (Fig. 14b):

$$v_{cc,i}(\zeta) = \int_{r_N}^{r_M} \sigma_\alpha(\zeta, r) \, \mathrm{d}r \cdot \frac{\sin\alpha}{E_c}$$
$$= \log\left(\frac{r_M(\zeta)}{r_M(\zeta)}\right) \cdot \sigma_{\alpha d} \frac{x_M(\zeta) + r_M(\zeta) \cdot \cot\alpha - x_E + r_E \cdot \tan\beta}{r \cdot (\tan\beta + \cot\alpha)} \cdot \frac{\sin\alpha}{E_c} \tag{25}$$

which, in turn, cause an axial interface slip at Rib *i*:

$$\delta_{R,i} = \frac{v_{cc,i}(\zeta)}{\tan\gamma_{rib}} \tag{26}$$

if one assumes that $v_{cc,i}$ is absorbed by sliding along the rib-concrete interface, i.e. associated by axial displacements such that concrete and reinforcing bar remain in contact (Fig. 14b). The corresponding reduction of the contact surface is included in the model, hence, less load is transferred as the contact surface becomes smaller with increasing interface slip.

The model assumes that the concrete between the conical compression fields does not contribute to the transfer of bond forces. However, this concrete constrains the relative displacements of adjoining conical compression fields, which complicates the superposition of the concrete displacements of the stress fields originating at all ribs. For simplicity, it is assumed here that (i) the radial displacements $v_{cc,i}$ and hence the axial interface slip $\delta_{R,i}$ at each rib depend only on the stress field at the corresponding rib, but (ii) the concrete parts between the conical compression fields impose the vertical displacements of the conical compression field at Rib $i + 1$ to that of Rib i. The axial concrete displacement at Rib i thus corresponds to the sum of the contributions of all stress fields between Rib i and the ideal cross-section.

In order to ensure that concrete and reinforcement remain in contact along the discontinuity surface BK, the axial steel displacements $u_{s,i}$ at each rib must correspond to the sum of the axial concrete displacements $u_{c,i}$ and the axial interface slip $\delta_{R,i}$, unless additional slip $\delta_{sp,i}$ occurs either due to internal splitting (causing concrete dilation enabling higher reinforcing bar slip at the interface) or local concrete crushing in front of the ribs, or both. As the stress field is derived rib-wise, starting at the main crack, the total steel displacement $u_{s,i}$ and the concrete displacements component $u_{c,i}$ – which are integrals of the steel and axial concrete deformations, respectively, from the ideal cross-section to the rib under consideration – are unknown until the entire stress field has been developed. Hence, an iterative solution would be required if the stress field depended on the total displacements, similar to the solution of the differential equation of bond in models relying on nominal bond shear stress-slip relationships. Note that in such models, the nominal slip δ is commonly defined as the difference between the total steel displacements u_s and the concrete elongation due to bond-induced axial
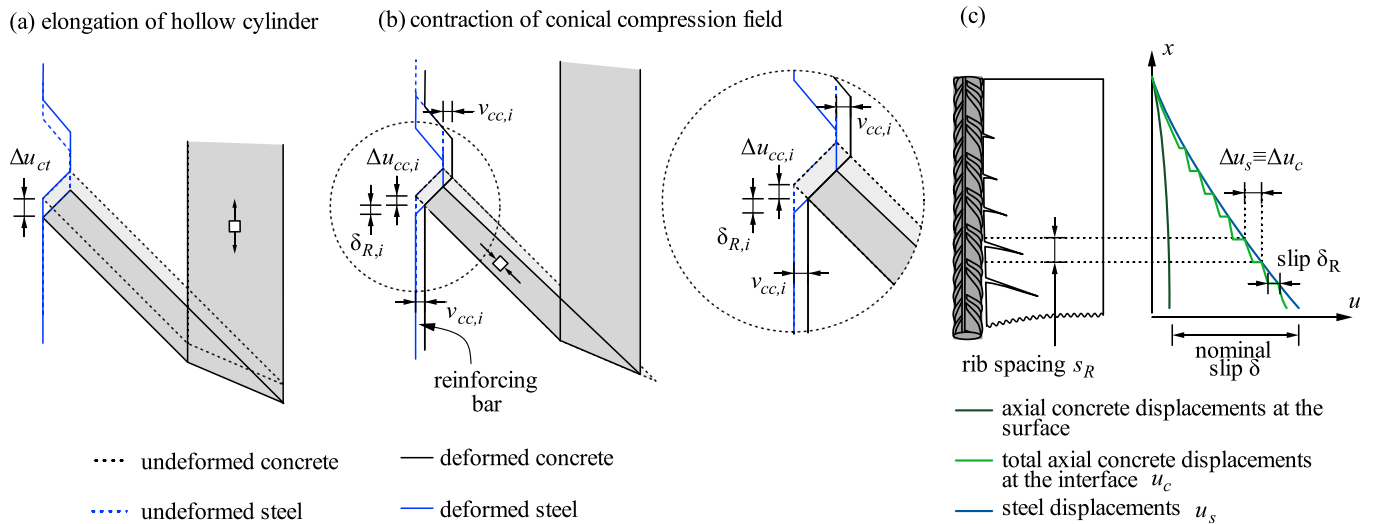
Fig. 14. Assumed concrete stress-induced interface displacements: (a) isolated hollow cylinder deformations; (b) conical compression field deformations; (c) displacements of the concrete at the surface, the concrete at the interface and the steel (neglecting additional slip due to splitting or local concrete crushing in front of ribs).

tensile stresses (see Fig. 14c), which essentially corresponds to the elongation of the hollow cylinders u_{ct} in the stress field model, i.e. the nominal slip $\delta = u_s - u_{ct}$ contains the stress-induced concrete displacements u_{cc}.

However, since (i) the total steel displacements $u_{s,i}$ and the axial concrete displacements $u_{c,i}$ are sums of the contributions of all stress fields between Rib i and the ideal section, and (ii) compatibility must be satisfied at all ribs, interface compatibility can also be formulated incrementally, i.e. in terms of steel and concrete displacement increments $\Delta u_{s,i}$ and $\Delta u_{c,i}$ between two successive Ribs i and $i + 1$ (Fig. 14a)

$$\Delta u_{s,i} = \Delta u_{cc,i} + \Delta u_{ct,i} + \delta_{R,i} + \delta_{sp,i} \qquad (27)$$

and as the stress field does not depend on the total steel or concrete displacements but only on their rib-wise increments, the stress field can be developed using incremental interface compatibility starting from the main crack. As the input values depend on the transferred load, ensuring equal displacement increments is a suitable condition for controlling the load transfer. A tolerance for the relative difference between Δu_s and Δu_c is introduced to account for imperfections and model insecurities, such as the assumed linear elastic concrete behaviour and the uncertainty arising from the expansion of the hollow cylinders carrying tensile stresses with regard to the position of the ideal section, which also improves the robustness of the numerical implementation.

4.2.2. Solution procedure

In the development of the stress field following the workflow illustrated in Fig. 11, it is initially assumed at each rib that all concrete displacement increments at the interface are stress-induced, i.e. caused by $\Delta u_{ct,i}$, $\Delta u_{cc,i}$ and $\delta_{R,i}$ (due to $v_{cc,i}$), hence $\delta_{sp,i} = 0$. If no stress field (i) complying with the boundary conditions and the yield criterion, as well

as (ii) satisfying interface compatibility with $\delta_{sp,i} = 0$ can be found, it is assumed that additional slip $\delta_{sp,i} > 0$ is caused by internal splitting cracks and local concrete crushing in front of the rib in order to satisfy displacement compatibility at the interface. This is typically the case if the reinforcing bar yields: bond stresses are low and the concrete stress-induced interface displacements including interface slip are small, while the steel displacements increase disproportionally.

The additional slip $\delta_{sp,i}$ required for interface compatibility is determined as the difference between steel and concrete displacements while maximising bond. However, since the additional slip ($\delta_{sp,i} > 0$) is associated with internal splitting, the concrete near the reinforcing bar is assumed to be radially cracked, and no triaxial stresses can develop at the reinforcing bar-concrete interface in this case. Hence, if $\delta_{sp,i} > 0$, γ is set equal to the rib flank inclination γ_{rib}. Note that higher bond stresses cause more pronounced steel stress changes and larger concrete stress-induced interface displacements requiring smaller additional slip and vice versa; the solution with maximum bond thus requires a minimum additional slip $\delta_{sp,i}$. Higher bond forces in parts affected by splitting could be ensured by providing confining reinforcement (similar as in the Dual-Cone stress field [45]), enabling a triaxial nodal zone despite internal splitting. This is, however, beyond the scope of this paper.

Unlike the rigid-plastic stress fields presented in Section 3, which are independent of the applied load as long as it is equal to or higher than the cracking load, the stress field with interface compatibility depends on the applied load. Thus, the numerical solution must be carried out step-wise with increasing loads. Thereby, the four stages shown in Table 2 are distinguished: (1) crack formation, (2) stabilised cracking, (3) elastic-cracked behaviour and (4) plastic steel deformations. In the crack formation stage (1), the concrete is assumed to be pre-cracked at large distances, resulting in a pull-out situation at the cracks. The crack spacing is determined for the cracking load (where cracking stabilises in

Table 2
Modelling stages for the stress field with interface compatibility depending on the cracking load F_{cr} and the steel yielding load F_{sy}.

Stage	Load	Characteristics
1 – crack formation (pull-out situation)	$F < F_{cr}$	Concrete not fully activated in tension. Ideal cross-section where steel and axial concrete strains are equal. Internal splitting may occur.
2 – stabilised cracking	$F = F_{cr}$	Concrete fully activated in tension. Cracks forming initially at the maximum crack spacing and subsequently at the minimum crack spacing. Internal splitting may occur.
3 – elastic-cracked	$F_{cr} < F < F_{sy}$	Minimum crack spacing from Stage 2 kept constant (formation of possible further cracks neglected). Internal splitting may occur, more likely near crack.
4 – plastic steel deformations	$F_{sy} < F$	Bond decreases with decreasing steel stiffness. Minimum crack spacing from Stage 2 kept constant. Internal splitting likely to occur.

load control) and subsequently kept constant, i.e. the concrete is not necessarily fully activated in tension for loads higher than the cracking load F_{cr}, as the bond stresses may decrease at higher load.

4.2.3. Results

The model extension with interface compatibility is validated against Specimen Ø16.M.ND#2 (Table 1) as this specimen is well-suited to investigate the occurrence of splitting. The four stages defined in Table 2 are represented by four different stress fields with interface compatibility, which were developed for maximum steel stresses (at the crack) of 200, 335, 450 and 580 MPa. The results obtained from the stress fields

with interface compatibility, the experimental data – again for all crack elements to illustrate the inherent scatter – and the TCM predictions are compared in Fig. 15.

The bond stress distributions (Fig. 15a) and average axial concrete stress distributions (Fig. 15b) obtained from the stress field with interface compatibility correlate well with the experimentally observed profiles, capturing both the ascending as well as the descending branches in the bond stress distributions; the latter is mainly enabled by the interface compatibility condition. The TCM overestimates the concrete stresses in all cases and provides reasonable average bond stresses, particularly at higher loads and for the elements that did not split, but
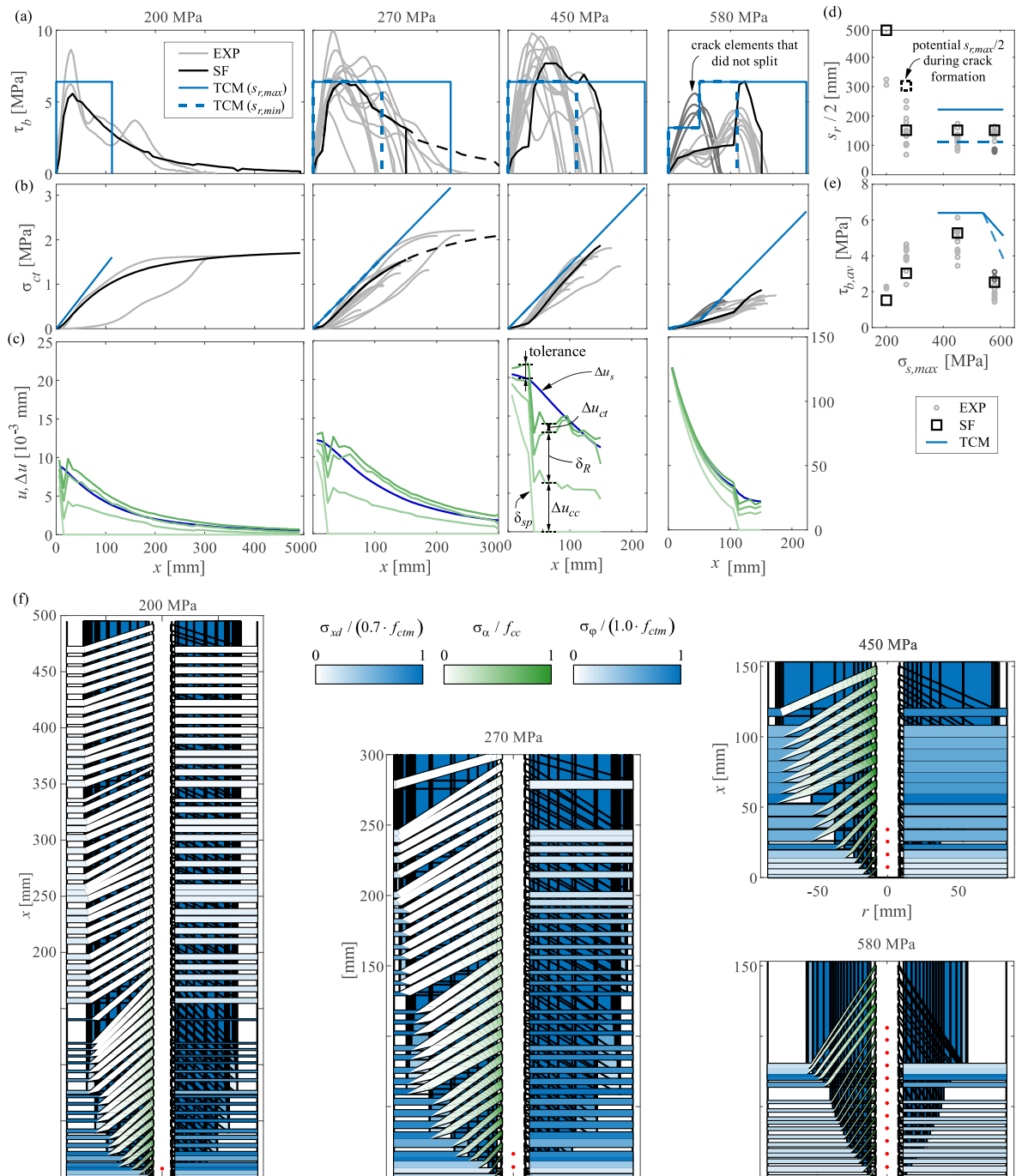

Fig. 15. Results of the stress fields with interface compatibility compared to experimental data and TCM predictions for Specimen Ø16.M.ND#2 at maximum steel stresses of 200, 270, 450 and 580 MPa: (a) bond stress distributions; (b) average axial concrete stress distributions; (c) displacements at the interface; (d) crack spacing and (e) average bond stresses; (f) stress field geometries with highlighted conical compression fields (left) and tensile rings (right) (ribs with splitting marked with red dots). (For interpretation of the references to colour in this figure legend, the reader is referred to the web version of this article.)

cannot account for the bond loss due to splitting. At low load during crack formation (pull-out situation at 200 MPa), the concrete was activated over a long distance which is captured well by the stress field model, while the Tension Chord Model – due to the assumed high bond stresses ($2 \cdot f_{ct}$) – activates a much shorter length. Note that the experimental data exhibit some bending effects presumably caused by the clamping of the steel bar ends [48].

The displacements illustrated in Fig. 15c indicate that controlling bond forces via interface compatibility worked well for all stages. The total steel and concrete displacements show a higher difference (corresponding to the admitted tolerance) at high bond stresses and also increasingly with high steel deformations (Stages 2 and 3). A possible explanation is that in such cases, concrete crushing would contribute to slip, which cannot be accounted for in the model, as it is only introduced together with splitting and $\gamma = \gamma_{rib}$. Note that already during crack formation (pull-out situation, see red dots for ribs with splitting in Fig. 15f) at 200 MPa, the slip contribution due to splitting was required at the first rib, where the steel displacement is largest while the length over which concrete can be compressed, i.e. generate $\Delta u_{cc,i}$ and $\delta_{R,i}$ (due to $\nu_{cc,i}$), is very short. For the same reason, branches with initial low bond stresses are also seen in Stages 2 and 3 (270 and 450 MPa). In Stage 4 (580 MPa) with plastic steel strains near the crack, longitudinal splitting was experimentally observed in all but four crack elements of the specimen. The bond stresses in the crack elements exhibiting splitting are modelled very well by the stress field, including the increase of bond stresses further away from the crack, although the longitudinal extent of the split region is slightly overestimated, which could be attributed again to the fact that the model assumes splitting as soon as $\delta_{sp} > 0$ is required for interface compatibility, but δ_{sp} could partly be caused by concrete crushing in front of the ribs without splitting and therefore higher bond stresses. On the other hand, the maximum bond stresses predicted by the model in the unsplit region are higher than experimentally observed. A possible explanation is that the confinement capacity of the annular discs providing confinement in the split region, was not reduced.

Fig. 15d and e illustrate the crack spacing and the average bond stresses. Concrete cracking occurred in the experiment at very low stresses of only 190 MPa, while the TCM predicts cracking at 380 MPa and the stress field at 266 MPa (assuming a tensile strength of $0.7 \cdot f_{ct}$). This can be explained by initial stresses due to shrinkage and possible bending effects, as well as scatter of the tensile strength. The TCM provides reliable lower and upper bounds for the crack spacing, but the local and the average bond stresses are overestimated, particularly for Stages 2 and 4, where they are overpredicted by a factor of 2…3. The stress field with interface compatibility activates the full axial concrete tensile capacity at around 270 MPa (see also Fig. 15f) where a new crack forms at $x = 300$ mm. This crack spacing is then held constant, as the stress fields for 450 and 580 MPa do not even activate the full tensile capacity at the given crack spacing, hence no new crack is predicted. The average bond stresses predicted by the stress field closely match the experimental data.

4.2.4. Discussion

Accounting for interface compatibility improves the capability of the stress field to predict the load-deformation behaviour while maintaining transparency and a clear physical meaning of all model components: Interface compatibility requires that the change in elongation of the reinforcing bar must be matched by the concrete stress-induced axial interface displacements, which are assumed to consist of the contraction of the conical compression field along its generatrices (causing axial and radial interface displacements, the latter being absorbed by interface slip) and the expansion of the axial hollow cylinder, with an additional slip due to internal splitting and crushing of the concrete in front of the ribs where required. With this simple condition, the load transfer could

be steered satisfactorily in dependence on the applied load. The results match the experimental data very well, and the occurrence of splitting cracks could be predicted in the specimen used for validation.

Nonetheless, the stress field still should be improved in some important aspects, particularly regarding the modelling of the splitting cracks and their radial extent. On the one hand, the concrete in the split region around the reinforcing bar cannot be activated tangentially, but at least in the specimen used for validation, the tangential stresses in the split region were very low (see Fig. 15f, 580 MPa), such that the surrounding concrete would likely be able to carry the radial bursting load, enabling higher stresses in the node ABK and thus higher bond stresses. In fact, rather than the capacity of the tensile hoops, the low bond stresses predicted by the model in the split area are primarily caused by the lack of a triaxial zone ABK at the ribs (imposing $\gamma = \gamma_{rib}$), which can diminish the bond stress by an order of magnitude at typical rib flank inclinations (see Fig. 5b). On the other hand, the model does not account for the fact that the tensile hoops confining the conical compression fields of the ribs adjacent to the split area with rather high bursting forces are located in the split region, which should reduce their capacity; as commented in Section 4.2.3, this may cause overprediction of the bond stresses near the split area.

Furthermore, as additional slip is needed to satisfy interface compatibility, splitting is introduced at low loads. This prevents the formation of a triaxial stress state near the ribs and leads to excessively low bond stresses in the region close to the crack. However, the missing slip is at least partly due concrete crushing, which is ignored by the model. Using a non-linear constitutive law for concrete could enhance the predictions by creating a transition from linear-elastic to fully split behaviour.

5. Summary of the main findings and conclusion

This paper investigates the load transfer between reinforcing steel and concrete with stress fields for the case of axisymmetric reinforced concrete (RC) ties subjected to monotonic loading. To this end, a rigid-plastic discontinuous stress field based on the lower bound theorem of Plasticity Theory (Section 3) was developed and subsequently refined and extended to account for interface compatibility (Section 4). Rather than relying on the crude idealisation of nominal bond shear stresses and slip and semi-empirical bond shear stress-slip relationships as most existing bond models, the stress fields presented in this paper derive the load transfer based on the material properties and geometry of the RC tie and the capability of the surrounding concrete to carry the loads. Bond forces are transferred through a triaxial nodal zone at the concrete-reinforcing bar interface and radially spread by hollow conical compression fields, whose radial and axial components are resisted by annular discs acting as hoops and axial hollow cylinders loaded in tension. The geometry of the stress field was developed such that critical overlap of stress field parts is minimised, and the inner radius of the annular discs and the smallest hollow cylinder defined such that the superposition of tensile stresses in these components with the compressive stresses in the conical compression field is not governing.

The rigid-plastic stress field, whose geometry is independent of the level of applied load, was validated against experimental data obtained from three RC ties instrumented with distributed fibre optical sensing (DFOS), showing good correlation in terms of the maximum bond stresses and crack spacing and highlighting that the stress field is capable of reliably accounting for the influence of the reinforcing bar diameter and rib geometry. However, the initial assumption that the tensile capacity of the hollow cylinders should be fully utilised by each individual conical compression field proved to be unfavourable in cases of high bond stresses, where concrete crushing in the conical compression field becomes governing, accompanied by a sudden drop in bond

stresses. Therefore, a local reduction of the axial tensile stresses in the hollow cylinders corresponding to the affected conical compression fields was explored in Section 4.1, yielding improved predictions of the behaviour. However, this solution is neither optimal for the stress field at an individual rib, nor for the global stress field, and the method requires further development.

While the rigid-plastic discontinuous stress fields, enhanced by the local reduction of axial tensile stresses where appropriate, provide good predictions of the bond strength, they cannot account for the influence of the applied load and steel strains, which is particularly relevant in the post-yield range. Therefore, an extension of the stress field with an interface compatibility condition, ensuring contact between the concrete and reinforcing steel at every rib for the load transfer, was explored. The extended model does not ensure rigorous deformation compatibility but maintains the clear mechanical meaning of all components as in the rigid-plastic stress field. The main findings and conclusions for the stress field with interface compatibility, which essentially corresponds to a Level 2 approximation according to [53], are:

- Despite the crude idealisation and simplistic interface compatibility condition, the predictions of the bond stress profiles – including the ascending and descending branches – and their dependency on the applied load or steel strains, respectively, could be greatly improved.
- The model is capable of capturing the local and average bond stresses and the crack spacing throughout the investigated loading stages – crack formation, stabilised cracking, cracked-elastic behaviour and post-yield range – satisfactorily, with its predictions correlating very well with experimental data.
- The model can predict the occurrence of internal splitting and the associated drop in bond stresses in the split region, and yields a mechanical explanation for the behaviour, i.e. the additional slip required to absorb large differences in steel and concrete displacements that cannot be accommodated by concrete stress-induced interface displacements, which could not be explained by simple equilibrium in the rigid-plastic model.
- The stress fields are highly valuable for visualising the flow of forces, and provide a clear mechanical explanation of the distribution of bond stresses, how confinement influences them, and what failure modes govern. One such example is the influence of the missing triaxial stress state in the case of splitting, where the omission of the triaxial nodal zone ABK adjacent to the ribs, explains the decrease in bond stresses.

In conclusion, the stress field with interface compatibility provides a proof of concept for the use of similar models in order to determine more realistic load-dependent bond stress distributions by approaching bond beyond its reduction to an interface property as common in nominal bond shear stress-slip models.

Future work could focus on the refined modelling of splitting, e.g. determining the extent of the split region based on the approaches by

Tepfers and Schenkel [35,37] to improve the modelling of concrete confinement within the split region. Also, an approach on how to separately include concrete crushing and splitting is desirable as slip caused by concrete crushing can maintain a triaxial nodal zone ABK. Furthermore, the stress field should be globally optimised, rather than carrying out local optimisations in its rib-wise development. Thereby, the axial concrete stress σ_{xd} could be globally optimised and compatibility could be accounted for in a more refined manner based on total displacements. In addition, the model should be extended to and validated for confined RC ties, accounting for the beneficial effect of transverse reinforcement not only acting as tensile hoops, but also providing additional confinement for the nodal zone ABK adjacent to the ribs (analogously as derived in [45]) thus enabling triaxial stress states in the case of splitting; however, suitable experimental data for validation is lacking. Another potential future work direction is a finite element implementation of a fully compatible stress field, similar to [33], with global optimisation. Compared to conventional finite element analyses, such a model would have the advantage of being suitable for parametric studies without the need for calibrated, empirical parameters of bond shear stress-slip relationships. Such analyses could be used for instance to determine the influence of the rib geometry on bond systematically and optimise it for specific applications.

CRediT authorship contribution statement

Tena Galkovski: Conceptualization, Validation, Investigation, Data curation, Writing – original draft, Visualization, Project administration, Software, Formal analysis. **Jaime Mata-Falcón:** Conceptualization, Writing – review & editing, Supervision. **Walter Kaufmann:** Writing – review & editing, Supervision, Funding acquisition.

Declaration of Competing Interest

The authors declare that they have no known competing financial interests or personal relationships that could have appeared to influence the work reported in this paper.

Data availability

Some or all data, models, or codes that support the findings of this study are available from the corresponding author upon justified request.

Acknowledgements

Appendix A

For the superposition of the conical compression field and the hollow cylinders subjected to uniaxial tension, basically two cases can be distinguished depending on the inclination of the compression field: (a) $\alpha \leq \pi/4 - \varphi/2$ and (b) $\alpha > \pi/4 + \varphi/2$ (see Fig. 16). In the first case (a), the conical compression superimposed to the axial tension is beneficial, and the superposition (even with fully activated uniaxial strengths in each component, i.e. $\sigma_\alpha (=\sigma_{\alpha0}) = f_c$ and $\sigma_{xd} = f_{ct}$) will not govern failure. In the second case (b), the conical compression needs to be reduced below its uniaxial capacity such that sliding failure is avoided (first Eq. (3), with $\sigma_3 = \sigma_\alpha$ and $\sigma_1 = f_{ct}$) [46]. For the most unfavourable angle $\alpha = \pi/2$, compressive stress within the region where the compressive and axial stress fields intersect must be limited to $f_{c,red}$ to avoid failure:

$$\sigma_\alpha = \left(\tan\varphi + \sqrt{1 + \tan^2\varphi}\right) \cdot \left[\left(\tan\varphi + \sqrt{1 + \tan^2\varphi}\right) \cdot f_{ct} - \frac{f_c}{2}\right] = f_{c,red} \tag{28}$$
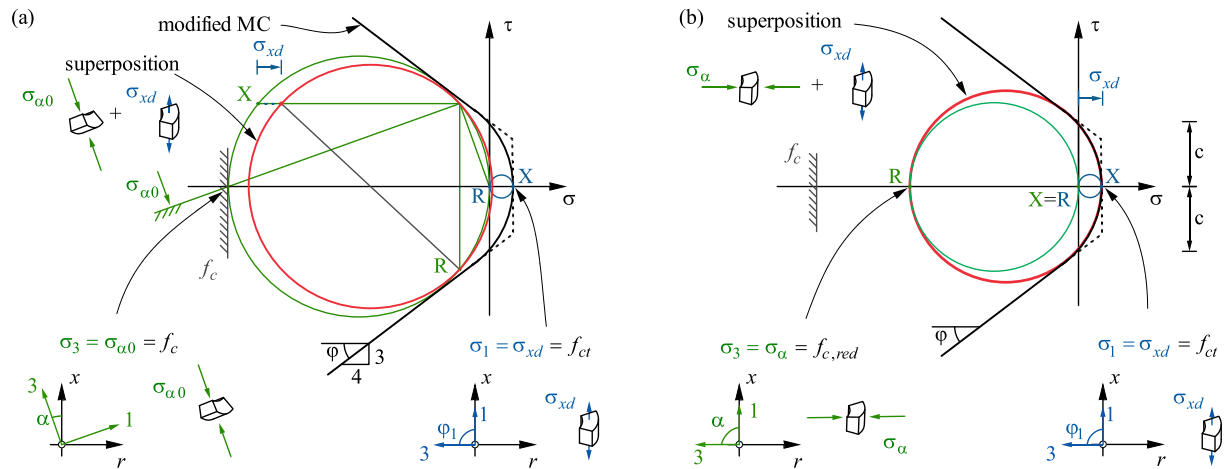
Fig. 16. Failure modes in regions where the conical compression field (green) is superimposed to the axial tension field (blue): (a) case with beneficial superposition of stress fields for $\alpha < \pi/4 - \varphi/2$; (b) case for $\alpha > \pi/4 + \varphi/2$ in which the axial tensile stress (uniaxial tensile strength) in the axial compression field reduces the compressive strength of the conical compression field below its uniaxial capacity.

For simplicity, only the latter case is considered in the development of the stress field. Since the compressive stresses in the conical compression field decrease with the radius, this criterion can indirectly be satisfied by choosing the inner radius of the axial tensile hollow cylinder activated by the first rib ($r_{ct,\min}$) such that the region where the stress fields intersect is not governing and hence, the conical compression field can be verified only by checking that its maximum stress (at the boundary BK of the triaxial nodal zone) is below its uniaxial compressive strength. This applies if $\sigma_\alpha(r_{ct,\min}) \leq f_{c,red}$, leading to Eq. (19).

Thereby, the inner part of the tie ($r < r_{ct,\min}$) carries no tensile stresses, since neither the axial tensile hollow cylinders nor the annular discs acting as hoops extend inside $r_{ct,\min}$. This is plausible since the transfer of tensile stresses is impeded by the conical micro-cracks (see Fig. 1b) that are likely to occur in this region already at low loads.

References

[1] International Federation for Structural Concrete. fib model code for concrete structures 2010. Berlin: Ernst & Sohn; 2013.

[2] European Committee for Standardization (CEN). Eurocode 2: Design of concrete structures - Part 1-1: General rules and rules for buildings (EN 1992-1-1:2004). Brussels, Belgium: 2005.

[3] ACI Committee 318. Building code requirements for structural concrete (ACI 318-08) and commentary. Farmington Hills, MI: American Concrete Institute; 2009.

[4] Marti P, Alvarez M, Kaufmann W, Sigrist V. Tension chord model for structural concrete. Struct Eng Int 1998;8:287–98. https://doi.org/10.2749/101686698780488875.

[5] Kuuskoski V. Über die Haftung zwischen Beton und Stahl ("On bond between concrete and steel"). Doctoral Thesis. The State Institute for Technical Research, 1950.

[6] Rehm G. Über die Grundlagen des Verbundes zwischen Stahl und Beton ("On the fundamentals of bond between concrete and steel") 1961;vol. Heft 138:p. 59 pp..

[7] Eligehausen R. Local bond stress-slip relationships of deformed bars under generalized excitations: experimental results and analytical model. Berkeley, California: Earthquake Engineering Research Center, College of Engineering, University of California; 1983.

[8] Lemcherreq Y, Zanuy C, Vogel T, Kaufmann W. Strain-based analysis of reinforced concrete pull-out tests under monotonic and repeated loading. Eng Struct 2023; 289:115712. https://doi.org/10.1016/j.engstruct.2023.115712.

[9] Hamad BS. Bond strength improvement of reinforcing bars with specially designed rib geometries. SJ 1995;92(3–13). https://doi.org/10.14359/1464.

[10] Darwin D, Graham EK. Effect of deformation height and spacing on bond strength of reinforcing bars. ACI Struct J 1993;90:646–57.

[11] Metelli G, Plizzari GA. Influence of the relative rib area on bond behaviour. Magaz Concr Res 2014;66:277–94. https://doi.org/10.1680/macr.13.00198.

[12] Gambarova PG, Rosati G. Bond and splitting in reinforced concrete: test results on bar pull-out. Mater Struct 1996;29:267–76. https://doi.org/10.1007/BF02486361.

[13] Mylrea TD. The carrying capacity of semicircular hooks. ACI J Proc 1928;24. https://doi.org/10.14359/15385.

[14] Posey CJ. Tests of anchorages for reinforcing bars. IowaCity: State University of Iowa; 1933.

[15] Bach C. Versuche mit Eisenbetonbalken ("Tests with reinforced concrete beams"). Berlin, Heidelberg: Springer Berlin Heidelberg; 1907. https://doi.org/10.1007/978-3-662-41212-1.

[16] Mains RM. Measurement of the distribution of tensile and bond stresses along reinforcing bars. J Proc 1951;48:225–52.

[17] Bresler B, Bertero V. Behavior of reinforced concrete under repeated load. J Struct Div 1968;94:1567–92. https://doi.org/10.1061/JSDEAG.0001981.

[18] Lagier F, Massicotte B, Charron J-P. Experimental investigation of bond stress distribution and bond strength in unconfined UHPFRC lap splices under direct tension. Cem Concr Compos 2016;74:26–38. https://doi.org/10.1016/j.cemconcomp.2016.08.004.

[19] Moreno DM, Trono W, Jen G, Ostertag C, Billington SL. Tension stiffening in reinforced high performance fiber reinforced cement-based composites. Cem Concr Compos 2014;50:36–46. https://doi.org/10.1016/j.cemconcomp.2014.03.004.

[20] Cantone R, Fernández Ruiz M, Muttoni A. A detailed view on the rebar–to–concrete interaction based on refined measurement techniques. Eng Struct 2021;226: 111332. https://doi.org/10.1016/j.engstruct.2020.111332.

[21] Kenel A. Biegetragverhalten und Mindestbewehrung von Stahlbetonbauteilen ("Flexural behaviour and minimum reinforcement of structural concrete members"). Doctoral dissertation. Institut für Baustatik und Konstruktion, ETH Zürich, 2002, doi: 10.3929/ethz-a-004488185.

[22] Mata-Falcón J, Haefliger S, Lee M, Galkovski T, Gehri N. Combined application of distributed fibre optical and digital image correlation measurements to structural concrete experiments. Eng Struct 2020;225:111309. https://doi.org/10.1016/j.engstruct.2020.111309.

[23] Fischer O, Thoma S, Crepaz S. Quasikontinuierliche faseroptische Dehnungsmessung zur Rissdetektion in Betonkonstruktionen ("Quasi-continuous fibre optical strain measurements for crack detection in structural concrete"). Beton- und Stahlbetonbau n.d.;114. doi: 10.1002/best.201800089.

[24] Quiertant M, Baby F, Khadour A, Marchand P, Rivillon P, Billo J, et al. Deformation Monitoring of Reinforcement Bars with a Distributed Fiber Optic Sensor for theSHM of Reinforced Concrete Structures. NDE, SEATTLE, United States: 2012, p. 10. https://hal.archives-ouvertes.fr/hal-01213089.

[25] Galkovski T, Lemcherreq Y, Mata-Falcón J, Kaufmann W. Fundamental studies on the use of distributed fibre optical sensing on concrete and reinforcing bars. Sensors 2021;21:7643. https://doi.org/10.3390/s21227643.

[26] Lemcherreq Y, Galkovski T, Mata-Falcón J, Kaufmann W. Application of distributed fibre optical sensing in reinforced concrete elements subjected to monotonic and cyclic loading. Sensors 2022;22:2023. https://doi.org/10.3390/s22052023.

[27] Ferreira M, Almeida J, Lourenço M. Avaliação do comportamento em serviço com modelos de campos de tensões contínuos ("Evaluation of the serviceability behaviour with continuous stress field models"). Revista portuguesa de engenharia de estruturas Serie III, N°18, March 2022. http://rpee.lnec.pt/.

[28] Lutz LA. Analysis of stresses in concrete near a reinforcing bar due to bond and transverse cracking. Am Concr Inst J Proc 1971:68. https://trid.trb.org/view/10228.

[29] Tammo K, Lundgren K, Thelandersson S. Nonlinear analysis of crack widths in reinforced concrete. Magazine Concr Res 2009;61:23–34. https://doi.org/10.1680/macr.2009.61.1.23.

[30] Lowes LN, Moehle JP, Govindjee S. Concrete-steel bond model for use in finite element modeling of reinforced concrete structures. SJ 2004;101:501–11. pp. 10.14359/13336.

[31] Jendele L, Cervenka J. Finite element modelling of reinforcement with bond. Comput Struct 2006;84:1780–91. https://doi.org/10.1016/j.compstruc.2006.04.010.

[32] Tan R, Hendriks MAN, Geiker M, Kanstad T. A numerical investigation of the cracking behaviour of reinforced-concrete tie elements. Magaz Concr Res 2020;72:109–21. https://doi.org/10.1680/jmacr.18.00156.

[33] Kaufmann W, Mata-Falcón J, Weber M, Galkovski T, Tran D.T, Kabelac J, et al. Compatible Stress Field Design of Structural Concrete: Principles and Validation. Zurich; Brno: ETH Zurich, Institute of Structural Engineering (IBK); IDEA StatiCa s. r.o.; 2020. https://www.research-collection.ethz.ch/handle/20.500.11850/411585.

[34] Mata-Falcón J, Tran DT, Kaufmann W, Navrátil J. Computer-aided stress field analysis of discontinuity concrete regions. In: Computational Modelling of Concrete Structures: Proceedings of the Conference on Computational Modelling of Concrete and Concrete Structures (EURO-C 2018), Bad Hofgastein, Austria: CRC Press; 2018, p. 641–50.

[35] Tepfers R. Cracking of concrete cover along anchored deformed reinforcing bars. Magaz Concr Res 1979;31:3–12. https://doi.org/10.1680/macr.1979.31.106.3.

[36] Martin H. Zusammenhang zwischen Oberflächenbeschaffenheit, Verbund und Sprengwirkung von Bewehrungsstählen unter Kurzzeitbelastung ("Relation between surface properties, bond and wedging action of reinforcing bars under short-term loading"). Berlin: Berlin, München, Düsseldorf: Dt. Ausschuss f. Stahlbeton; W. Ernst [in Komm.]; 1973.

[37] Schenkel M. Zum Verbundverhalten von Bewehrung bei kleiner Betondeckung ("On the bond behaviour of reinforcing bars with small concrete cover"). Doctoral thesis. ETH Zürich, Institut für Baustatik und Konstruktion, 1998. doi: 10.3929/ethz-a-002000034.

[38] Marti P. Theory of structures: fundamentals, framed structures, plates and shells. First ed. Berlin, Germany: Wiley Ernst & Sohn, A Wiley Company; 2013.

[39] Westergaard HM. On the method of complementary energy. Trans Am Soc Civil Eng 1942;107:765–93. https://doi.org/10.1061/TACEAT.0005550.

[40] Lourenço MS, Almeida JF. Adaptive stress field models: formulation and validation. ACI Struct J 2013;110:71–81.

[41] SIA. Swisscode SIA 262: Concrete Structures. Zurich, Switzerland: Swiss Society of Engineers and Architects (SIA); 2013.

[42] International Federation for Structural Concrete. In: fib Bulletin 10. Bond of reinforcement in concrete: state-of-art report. Lausanne: International Federation for Structural Concrete; 2000.

[43] Roš MGR. Die materialtechnischen Grundlagen und Probleme des Eisenbetons im Hinblick auf die zukünftige Gestaltung der Stahlbeton-Bauweise ("The material-specific fundamentals and problems of reinforced concrete with regard to the future design of structural concrete"). Zürich: Eidgenössische Materialprüfungs- und Versuchsanstalt für Industrie, Bauwesen und Gewerbe (EMPA); 1950.

[44] Muttoni A, Schwartz J, Thürlimann B. Design of concrete structures with stress fields. Basel: Birkhäuser Basel 1996. https://doi.org/10.1007/978-3-0348-9047-2.

[45] Markić T, Morger F, Kaufmann W. Partially loaded areas in reinforced concrete: Mechanical modelling. Eng Struct 2022;271. https://doi.org/10.1016/j.engstruct.2022.114938.

[46] Nielsen MP, Hoang LC. Limit Analysis and Concrete Plasticity, Third ed. Boca Raton: CRC Press; 2011. Doi: 10.1201/b10432.

[47] Harrild Sørensen J, Danmarks Tekniske Universitet, DTU Byg. Design and modeling of structural joints in precast concrete structures: Ph.D. thesis. Lyngby: DTU Civil Engineering; ISBN: 9788778774798; 2018.

[48] Galkovski T, Mata-Falcón J, Kaufmann W. Experimental investigation of bond and crack behaviour of reinforced concrete ties using distributed fibre optical sensing and digital image correlation. Eng Struct 2023;292:116467. https://doi.org/10.1016/j.engstruct.2023.116467.

[49] Christiansen M.B. Materialer DTUI for BK Og, DTU, Materials TU of DD of SE and. Serviceability Limit State Analysis of Reinforced Concrete. ISBN: 978-87-7740-279-1. 2000.

[50] Marti P. Zur plastischen Berechnung von Stahlbeton ("On the plastic design of structural concrete"). vol. 104. Basel, Switzerland: Birkhäuser; 1980.

[51] Plizzari G, Cairns J, Metelli G, Aiello MA, Bošnjak J, Centonze G, et al. fib Bulletin 106. Advances on bond in concrete. *fib*. The International Federation for Structural Concrete; 2022. https://doi.org/10.35789/fib.BULL.0106.

[52] Goto Y. Cracks formed in concrete around deformed tension bars. JP 1971;68:244–51. pp. 10.14359/11325.

[53] Passos Sério Lourenço MF, Fernández Ruiz M, Haugerud SA, Blaauwendraad J, Bousias S, Hoang LC, et al. fib Bulletin 100. Design and assessment with strut-and-tie models and stress fields: from simple calculations to detailed numerical analysis. The International Federation for Structural Concrete; 2021. https://doi.org/10.35789/fib.BULL.0100.

[54] Ramberg W, Osgood WR. Description of stress-strain curves by three parameters. n. d. https://ntrs.nasa.gov/citations/19930081614.